SANDIA REPORT
SAND200X-XXXX
Unlimited Release
Printed September 2015

A Study of the Optical Properties of Ice Crystals with Black Carbon Inclusions

Marco Arienti, Xiaoyuan Yang, Adrian Kopakz, and Manfred Geier

Prepared by
Sandia National Laboratories
Albuquerque, New Mexico 87185 and Livermore, California 94550

Sandia National Laboratories is a multi-program laboratory managed and operated by Sandia Corporation, a wholly owned subsidiary of Lockheed Martin Corporation, for the U.S. Department of Energy's National Nuclear Security Administration under contract DE-AC04-94AL85000.

Sandia National Laboratories

Issued by Sandia National Laboratories, operated for the United States Department of Energy by Sandia Corporation.

Available to DOE and DOE contractors from
U.S. Department of Energy
Office of Scientific and Technical Information
P.O. Box 62
Oak Ridge, TN 37831

Telephone: (865) 576-8401
Facsimile: (865) 576-5728
E-Mail: reports@osti.gov
Online ordering: http://www.osti.gov/scitech

Available to the public from
U.S. Department of Commerce
National Technical Information Service
5301 Shawnee Rd
Alexandria, VA 22312

Telephone: (800) 553-6847
Facsimile: (703) 605-6900
E-Mail: orders@ntis.gov
Online order: http://www.ntis.gov/search

SAND200X-XXXX
Unlimited Release
Printed September 2015

A Study on the Optical Properties of Ice Crystals with Black Carbon Inclusions

Marco Arienti, Xiaoyuan Yang, Adrian Kopakz, and Manfred Geier,
Thermal Fluid Science & Engineering
Sandia National Laboratories
Livermore, California 94550-MS905/2

Abstract

The report focuses on the modification of the optical properties of ice crystals due to atmospheric black carbon (BC) contamination: the objective is to advance the predictive capabilities of climate models through an improved understanding of the radiative properties of compound particles. The shape of the ice crystal (as commonly found in cirrus clouds and contrails), the volume fraction of the BC inclusion, and its location inside the crystal are the three factors examined in this study. In the multiscale description of this problem, where a small absorbing inclusion modifies the optical properties of a much larger non-absorbing particle, state-of-the-art discretization techniques are combined to provide the best compromise of flexibility and accuracy over a broad range of sizes.

ACKNOWLEDGMENTS

Support by Sandia National Laboratories' LDRD (Laboratory Directed Research and Development) is gratefully acknowledged. Sandia National Laboratories is a multi-program laboratory managed and operated by Sandia Corporation, a wholly owned subsidiary of Lockheed Martin Corporation, for the U.S. Department of Energy's National Nuclear Security Administration under contract DE-AC04-94AL85000.

CONTENTS

FIGURES

TABLES

NOMENCLATURE

dB	decibel

1. INTRODUCTION

The optical properties of atmospheric ice crystals play a fundamental role in modeling earth's radiation and hydrological cycle. Using an ensemble of thousands of general circulation model (GCM) simulations, a study by Sanderson (2008) identified the ice crystal fall speed, which is a function of ice crystal diameter and shape, as one of the dominant physical processes that can lead to variations in climate sensitivity. In turn, atmospheric black carbon (BC) is recognized as the dominant light absorbing aerosol particles with positive radiative forcing (warming) (Ramanathan & Carmichael 2008). However, in-situ observations (Cappa *et al.* 2012) indicate that the characterization of the mixing state of BC with ice crystals and other non-BC particles in global climate models needs further investigation. Since BC is small compared to ice crystals and other dust particles, and scattering cross sections are proportional to volume squared in the Rayleigh limit and size squared in the geometrics optics limit, hardly any effect on the atmospheric scattering characteristics can be expected. Therefor this work is mainly concerned with the strong absorption properties of light in a wide spectral range and with the fact that embedding into ice can magnify its absorption cross-section. Computationally, the study of compound ice-BC particles remains a challenging task because of the variability of crystal shapes and BC inclusion modes, as well as the drastically different absorbing properties of BC compared to ice in the visible range.

According to the estimate on BC inclusion in snow packs reported by Flanner et al. (2012), each ice grain could contain from 0.05 to 10^9 BC particles, possibly distributed as multiple inclusions within ice grains. In water drops, an accepted carbon volume fraction interval is between 10^{-7} and 10^{-3} (Chy'lek et al.,1984): for volume fractions larger than 10^{-3}, the specific absorption of carbon particles by water is expected to decrease rapidly because of the screening effect of too many carbon particles within the same drop.

The optics of BC residing within cloud droplets (e.g., Danielsen et al. 1969; Chy´lek et al., 1984, 1996; Fuller, 1995; Videen and Chy´lek, 1998; Jacobson, 2006) has been investigated by assuming a spherical shape: the mean estimates of absorption enhancement ranged between a factor of 1.5 to 3, depending on the inclusion optical properties and the size and spatial distribution of the inclusions. For ice crystals the shape characterization needs to be compared to the inclusion distribution. Scattering is rather insensitive to particle shape when its characteristic length, a, is smaller than the incident wavelength $X = 2\pi a/\lambda < 1$. Only the largest-scale deviations from the spherical shape, such as the aspect ratio, may be significant (e.g., Nousiainen et al., 2001) and, since the internal inhomogeneities is necessarily much smaller, an effective-medium approximation (EMA) can be expected to perform well (unless the inhomogeneity is very ordered, such as a coating on a particle). As the particle's size parameter X increases, relatively smaller-scale details in the particles become important. For wavelength-scale particles, the internal inclusion distribution is expected to become more relevant. A volume-integral method, such as the discrete-dipole approximation (DDA) used for this work, can be used to investigate this transition in detail. But methods that can account explicitly for the impact of wavelength-scale particle details are lacking when the particles themselves are considerably larger than the wavelength (e.g., Nousiainen, 2009). At sufficiently large size parameters (> 500), scattering becomes increasingly sensitive to shape, making geometrical optics (or ray tracing, RT) techniques more appealing. Unfortunately, the intermediate size parameters between the resonance and the geometric-optics domains remain a territory difficult to explore, although a promising numerical approach has emerged recently (Bi et al., 2013).

This situation justifies a careful study of mixing models for a realistic representation of the optical properties of this specific aerosol population. After a brief description of the physics of ice crystal formation and BC inclusion, we describe the two distinct numerical techniques (belonging to the DDA and RT methodologies) that were used in the limits of small and large size parameter, respectively. DDA and RT results are compared at one intermediate size parameter for verification purposes. Results for simple crystal shapes with BC inclusions are then compared with new measurements from a polarization spectrometer under controlled temperature, humidity and flow conditions. In their own respect, the experimental data provide useful insight of the relative importance of BC and crystal size in backward polarization intensity. Moreover, although the actual shape of the compound particles (and the position of the BC inclusions) could not be precisely known form the experiment, this validation effort is one of the few the authors are aware of in the context of atmospheric particles. Previous results in the literature indicate that a black carbon particle is more efficient in absorbing light when it is embedded in an ice crystal (e.g. Flanner *et al.* 2012), due to the effective focusing of incident light by the crystal. While it also has been reported that particles close to the surface are less efficient in this regard than inclusion further away from the crystal surface, little quantitative results have been reported as to effect of distances between inclusion and crystal face. Parametric studies are carried out to investigate this effect by examining the scattering properties of the compound particles for fixed shape and varying BC inclusion position and for fixed centered position and varying crystal shape.

1.1. Atmospheric ice particle habits

Atmospheric ice crystals are generally found in cirrus and stratus clouds. As their formation and growth depends on the highly variable conditions found in the atmosphere, ice crystals tend to take on a wide variety of shapes, or habits. In the airborne data collected using the Cloud Particle Imager (Korolev *et al.* 1999), only 3% of the particles were in "pristine" shape, with regular column, needle, plates and dendrites geometries. The remaining 97% of crystals were irregular faceted polycrystallines, or sublimating ice particles with smooth curving sides and edges, or aggregates of columns and plates (Heymsfield & Iaquinta 2000; Yang *et al.* 2013). The size of the ice crystals also exhibits a strong spatial and temporal variability, as shown for instance in data from the International Cirrus Experiment (ICE) or from the First International Satellite Cloud Climatology Project (ISCCP) Regional Experiment (FIRE; Kinne *et al*. 1997). A comprehensive habit diagram (Bailey & Hallett 2009) for atmospheric ice crystals, combining laboratory, field campaign, and studies from other fields, confirms that ice crystals are not only non-spherical, but also non-axially symmetric. Still, spheroidal or cylindrical approximations have often been assumed for crystal geometries (Mishchenko & Sassen 1998; Lee *et al.* 2003; Nicolet *et al.* 2012), in part because of lack of reliable shape distribution descriptions. Other representative geometries, such as hexagonal columns, plates, droxtals, hollow columns, and bullets were examined by Bi & Yang (2014); see also references therein.
Recent studies have proposed fractal-based techniques to generate crystal shapes that are more in agreement with empirical correlations between the effective diameter and the mass of retrieved crystals. The resulting optical properties seem to be in better agreement with atmospheric measurements (Ishimoto et al., 2012). The resulting shapes are in general more complex and do not typically exhibit halo effects and the enhancement at 150^{o}. An insertion procedure that mimics the process of formation by conglomeration of a falling crystal was proposed by Schmitt

and Heymsfield (2010). The simpler procedure by Ishimoto et al. (2012), based on the combination of Voronoi cells generated from an assigned fractal dimension seems to yield similar geometrical properties and it is adopted in the following for some of the ray-tracing calculation. An example of an individual Voronoi cell and of an assemblage of cells is displayed in Figure 1.

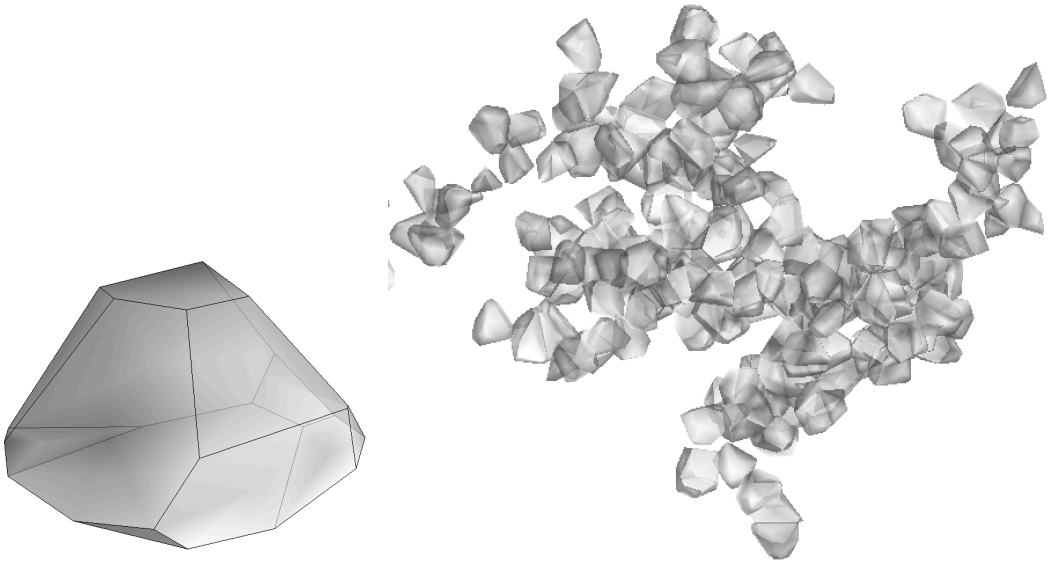

Figure 1. Single Voronoi cell and assemblage of cells.

1.2. BC inclusion mechanism

After being generated by emission, BC particles coagulate to form aggregates or chain-like structures consisting of hundreds or thousands of spheres (Lahaye & Ehrburger-Dolle 1994; Schwarz *et al.* 2006). The morphology of the aggregate structures evolves in time ("aging") in a manner that is very relevant to the optical characteristics of soot (Chen *et al.* 1990). The morphology of dry soot aerosol can be represented by a fractal cluster according to the scaling law below (Mikhailov *et al.* 2001; Sorensen 2001; Bond *et al.* 2013). Flanner *et al.* (2012) described in detail the mechanism of black carbon (BC) getting into ice particles. BC particles are hydrophobic when freshly emitted particles, but they rapidly "age" through the condensation of sulfuric acid and semi-volatile organics and coagulate with each other as well as other aerosols. The coating of condensed sulfates increases the hygroscopicity and attracts water to nucleate cloud droplets. Then, depending on the environment temperature, these BC nucleated cloud droplets can either be riming onto mature ice crystals, or become a part of the ice through aggregation and accretion, or grow from diffusive vapor through the Bergeron-Findeisen process. Thus, the possibility of containing multiple BC aggregates inside the single ice particle can be quite high, but it is hard to predict where they may be located.
Field measurements of bulk BC/snow indicate mass concentrations that are smaller than 10^{-5} (e.g., Clarke and Noone, 1985; Warren and Clarke, 1990; Doherty et al., 2010; Huang et al., 2011); individual ice grains may contain much larger BC volume fractions than the mean snowpack concentration.

The scattering phase function of cloud particles is highly dependent on the particle shape and size distribution (Kaufman *et al.* 1994). For an ice grain radius of 100 μm and monodisperse BC size distribution, Chy´lek et al. (1984) calculated an absorption enhancement factor of about 1.7 for realistic values of BC volume fractions; in that study BC particle size distribution was indicated as the largest source of uncertainty. Particles attached to the outside of weakly absorbing spheres cause enhancements that are negligible to weak (1.0–1.3) (e.g., Fuller et al., 1999; Liou et al., 2011).

2. OPTICAL ANALYSIS OF ICE CRYSTALS WITH BC INCLUSIONS

Various simplified model geometries have been applied on weekly absorbing aerosols that encapsulate absorbing BC (Kahnert *et al.* 2013). The simplest model treats BC and ice or other weakly absorbing aerosols as externally mixed, i.e., homogeneous spheres with no interaction. Alternatively, the two components can be treated as completely mixed spheres with an effective refractive index (Videen & Chýlek 1998; Chýlek *et al.* 2000). Another simple model for an encapsulated aerosol is the core-shell, consisting of an absorbing spherical core concentrically coated with a spherical shell of weakly absorbing material. A common simplification is to approximate irregularly shaped particles such as ice crystals and black carbon fractal aggregates as homogeneous, optically inactive (isotropic) spheres. This approximation permits utilization of analytical solutions in order to compute the spatial distribution of scattered electromagnetic radiation, as well as scattering and absorption cross-sections. For cases where irregular shapes are involved, Liou et al. (2011) linearly combined the geometric optics term (reflection/refraction and diffraction) with a surface-wave adjustment.

When the interaction between inclusions and crystal needs to be examined at scales that are comparable or smaller with respect to the incident wavelength, the discrete dipole approximation (DDA) is our preferred approach. DDA was first proposed by Purcell and Pennypacker (1973) and rigorously developed in a number of studies (Draine 1988; Draine & Goodman 1993; Flatau & Draine 1994; Draine 2000) over the past four decades. In this method, the volume of the scatterer is divided into small cubical sub-volumes, or dipoles, which interact with each other and the incident field. The resulting internal field, or its direct derivative, polarization, is solved by matrix inversion. Thus, DDA methods can accurately calculate light scattering and absorption by a target with arbitrary geometry with small parameter size. However, when orientation averaging is necessary, DDA methods require an increasing computational effort for increasing size parameters. The specific software used in this work is the Amsterdam Discrete Dipole Approximation (ADDA) software (Yurkin & Hoekstra 2013). By running on a multiprocessor system (with the Message Passing Interface protocol), ADDA can effectively increase the turnaround time of a simulation and extend the range of this technique to compound particles with larger size parameters. Verification tests are described in Appendix B.

The sizes of most ice crystals within cirrus clouds are on the order of several tens and hundreds of microns, therefore the corresponding size parameters in the solar spectral region are in the geometric optics regime. However, soot inclusion introduces smaller scales and the need to capture internal diffraction. It is then convenient to describe each BC particle in an ice crystal as a spherical monomer of radius a (Sorensen, 2001). A uniform electro-magnetic field exists across the monomer if the following conditions for a Rayleigh scatterer are met:

$$ka \ll 1; \qquad |m|ka \ll 1, \tag{1}$$

where $m = n + ik$ is the complex refractive index of the monomer. It is noted that a more accurate representation of inclusion aggregates could be carried out based on the stochastic procedures using homogeneous and core-shell spheres with smooth or rough surfaces as building blocks of carbon inclusions following Liou et al (2011).

We extended the Monte-Carlo ray-tracing (RTMC) code by A. Macke to enable the positioning of a finite number of spherical inclusions at fixed locations inside a crystal. The original RTMC code was described and utilized in a number of publications (e.g. Macke 1993, Macke *et al.* 1996, Macke *et al.* 1996b). The algorithm was modified to enable the specification of the locations of spherical inclusions within the crystal. This new code (labeled RTMCX) permits the evaluation of the effect of location and size of a small, fixed number of internal scatterers on the overall optical properties of the compound particle. Rather than using a specified free-mean path and a random number to determine the distance between internal extinction events (as in Macke *et al.* 1996), RTMCX relies on user-specified extinction cross-sections to define a circular "collision" cross-section for the ray. When a ray encounters an inclusion, the two angles defining the direction of the scattered ray are determined in a Monte Carlo procedure from the specified angular distribution of scattered intensities and the polarization state of the ray incident on the inclusion, following the procedure outlined in Muinonen *et al.* 2009. Data for the inclusion are pre-calculated and stored in a table.

The most significant feature introduced in RTMCX involves the determination of the complete phase matrix of the scatterer. This procedure involves tracking the Stokes vectors of collected light in both azimuthal (scattering) and polar angle bins for four different incident polarization states. Rays collected in the same angle bin are superposed, provided that the polarization state (Stokes vector) of the causing incident ray is the same. For a particular scattering direction (ϑ, φ), the relationship between the Stokes vectors of the incident rays and the emerging rays can be expressed as

$$(\boldsymbol{I}_1, \boldsymbol{I}_2, \boldsymbol{I}_3, \boldsymbol{I}_4)_{sca}(\vartheta, \varphi) = \boldsymbol{P}(\vartheta)\boldsymbol{L}(\varphi)(\boldsymbol{I}_1, \boldsymbol{I}_2, \boldsymbol{I}_3, \boldsymbol{I}_4)_{inc} \quad (2)$$

where $\boldsymbol{I}_j$ is the Stokes vector corresponding to the *j*-th incident Stokes vector (in column notation). The unknown phase matrix $\boldsymbol{P}(\vartheta)$ follows by solving the linear system of equations $\boldsymbol{Y} = \boldsymbol{PX}$, where $\boldsymbol{Y}$ is a 4-by-4*n* matrix composed of the 4-by-4 matrices for each polar angle φ, and $\boldsymbol{X}$ is the corresponding matrix compiled of rotated incident Stokes vectors $\boldsymbol{X} = \boldsymbol{L}(\varphi)(\boldsymbol{I}_1, \boldsymbol{I}_2, \boldsymbol{I}_3, \boldsymbol{I}_4)_{inc}$ (the definition of the rotation matrix $\boldsymbol{L}(\varphi)$ can be found in Mishchenko *et al.* 2000). Under the assumption that the phase matrix has the structure of randomly oriented particles, the 10 independent phase matrix elements of the phase matrix $\boldsymbol{P}$ are determined by linear regression ($\boldsymbol{P} = \boldsymbol{YX}^t (\boldsymbol{XX}^t)^{-1}$).). Next, assuming that the observed Stokes vectors are random variables with equal variances, the uncertainties in the estimated phase matrices are computed. The output is a valid Mueller matrix that is calculated for each scattering angle ϑ by the eigen-decomposition of the coherency matrix (Hovenier *et al.,* 1996).

Results are valid only in the large-parameter size limit: the extinction coefficient is hard-wired to 2, the large-size limit value (Bohren et al., 1983). As an example of the verification tests for RTMCX, we report the comparison of results for a large homogenous sphere with the results from Mie-scattering theory; see Figure 2. The size parameter of this test was $X = 10000$ and the refractive index of the scatterer was $m = 1.3117 + i0.0$. The analytical solution (Mie) was averaged over 1° angle intervals to match the angle bins used with the ray tracing software. The

sphere was approximated by a polyhedron with 36, 1088, and 10224 triangles. Approximations with 1088 and 10244 faces yielded less than 1% deviation of total scattering cross-sections and asymmetry factors with respect to the analytical values; using 36 faces caused relative errors of 15% and 6% for total scattering cross section and asymmetry factor, respectively. RTMCX simulations used 1000, 100, and 10 random orientations for the approximations with 36, 1088, and 10224 faces, respectively (1000 rays were used for each orientation). The plots of the nonzero elements in Figure 2 show that the agreement with the analytical solution improves with the increasing number of faces, in particular at scattering angles less than 90°. The angular dependence of the element Z_{11} was captured even for scattering angles reaching far backwards to about 170°, which is remarkable given variation of Z_{11} over four orders of magnitude. The other nonzero elements Z_{12}, Z_{22}, Z_{33}, Z_{34}, and Z_{44}, relative to Z_{11}, were captured less closely and exhibited larger local variability. This variability can be attributed to insufficient coverage due to the randomness of the Monte Carlo method.

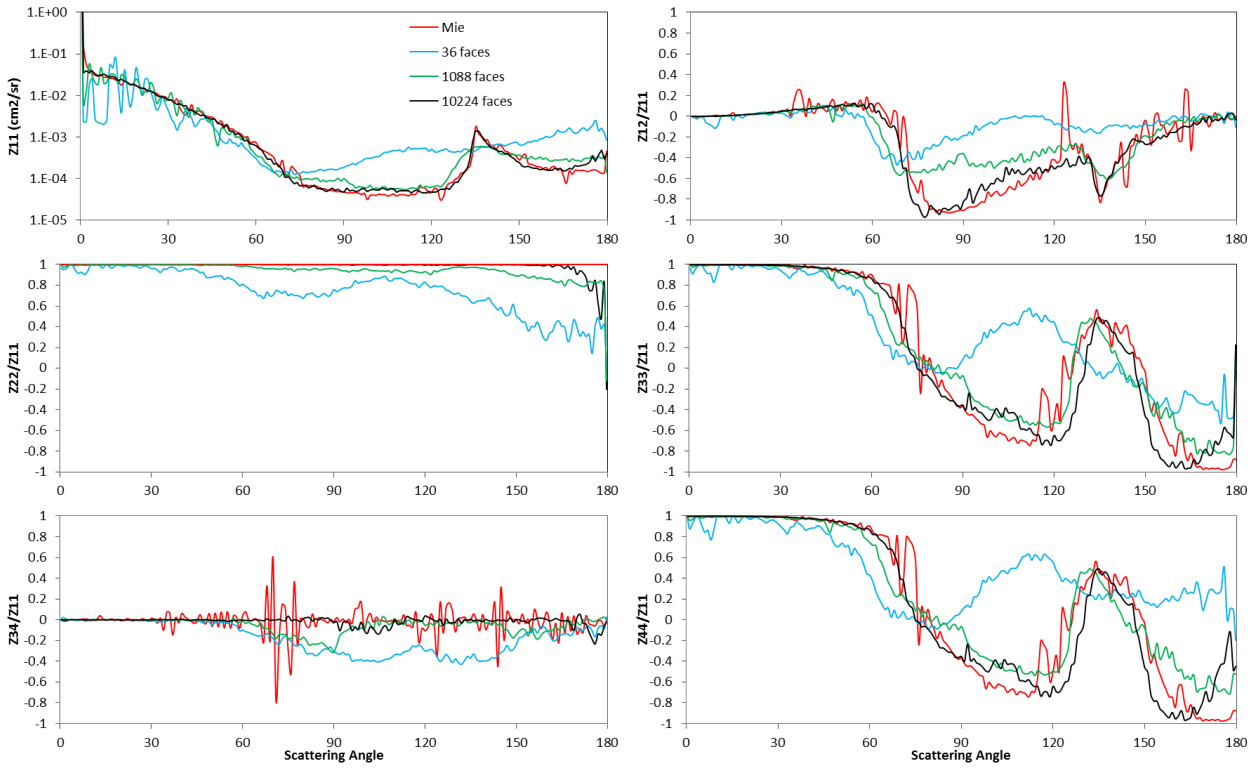

Figure 2. Nonzero elements of the scattering phase matrices for a large sphere. The reference phase matrix from the analytical solution (Mie, red line) is compared with the RTMCX elements obtained from a tessellation of the sphere with 34, 10024 and 10234 faces.

A second test consists in the direct comparison between ADDA and RTMCX phase matrices to cross-verify both computational approaches. This test is challenging because the assumptions RTMCX is based on begin not to be valid when the size parameter is less than 500, while with a large parameter size particle the ADDA calculation may stop converging. In the case of a

hexagonal prism shape, the maximum parameter size for which we could achieve a complete ADDA calculation was $X = 50$ (hexagonal pure ice crystals with L/D = 1, D = 9.79 μm, λ = 660 nm, refractive index $m_{ice} = 1.3117 + i0.0$). The lengthy operation of averaging the phase matrix for random orientations required a process to separate α-averaging, which is relatively inexpensive, from β- and γ-averaging. The latter operation was subdivided in N concurrent evaluations by sampling the angles β and γ. To improve efficiency we used two pseudo-random sequences of Halton numbers (β_i, γ_i) $i = 1 \ldots N$, (a Halton sequence typically provides a better sampling than purely random sampling, see Penttil and Kumme (2011)). The convergence rate of the quadrature was improved by using as weights the values of the areas A_i corresponding to the Voronoi tessellation on a unit sphere the (β, γ) sequence (thanks to John Burkard, FSU, for providing matlab functions): $\omega_i = A_i/(4\pi)$.

With $N = 129$, the scattering coefficient was $Q_{ext} = 1.3$ ($C_{ext} = 122.4$), that is, quite different from the limit value 2. The angular distributions of the scattering phase matrix elements from ADDA are shown in Figure 3. The matrix elements Z_{13}, Z_{14}, Z_{23}, Z_{24}, Z_{31}, Z_{32}, Z_{41}, and Z_{42} average to zero regardless of the scattering angle because of the symmetry properties of the crystal (Mishchenko *et al.* 2000). We overlap to these functions the phase matrix from RTMCX for the same shape: the match for the two curves is fairly good. Looking at the plot of Z_{11}, we see that ray tracing recovers the two ice halos at 22° and 46° (Bohren et al., 1983). These features may be exaggerated, as suggested by the comment of Macke and Mishchenko (1999) that well-defined halos should not be prevalent for size parameters less than 100. From benchmark calculations for the same crystal geometry, Bi *et al.* (2014) also indicate that ice halos from geometric optics are too prominent for a parameter size as large as 120. The two halos are greatly smoothed in the ADDA results (although some of the smoothing may also be caused by ADDA's approximation of sharp edges through dipoles).

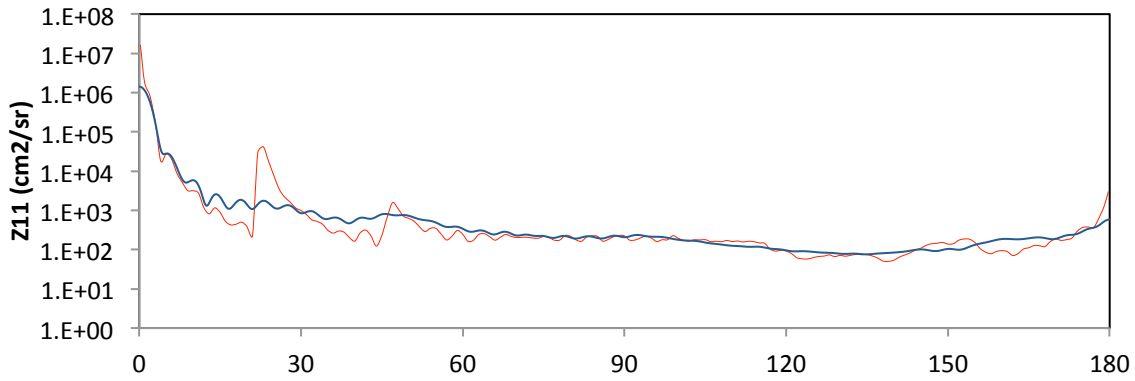

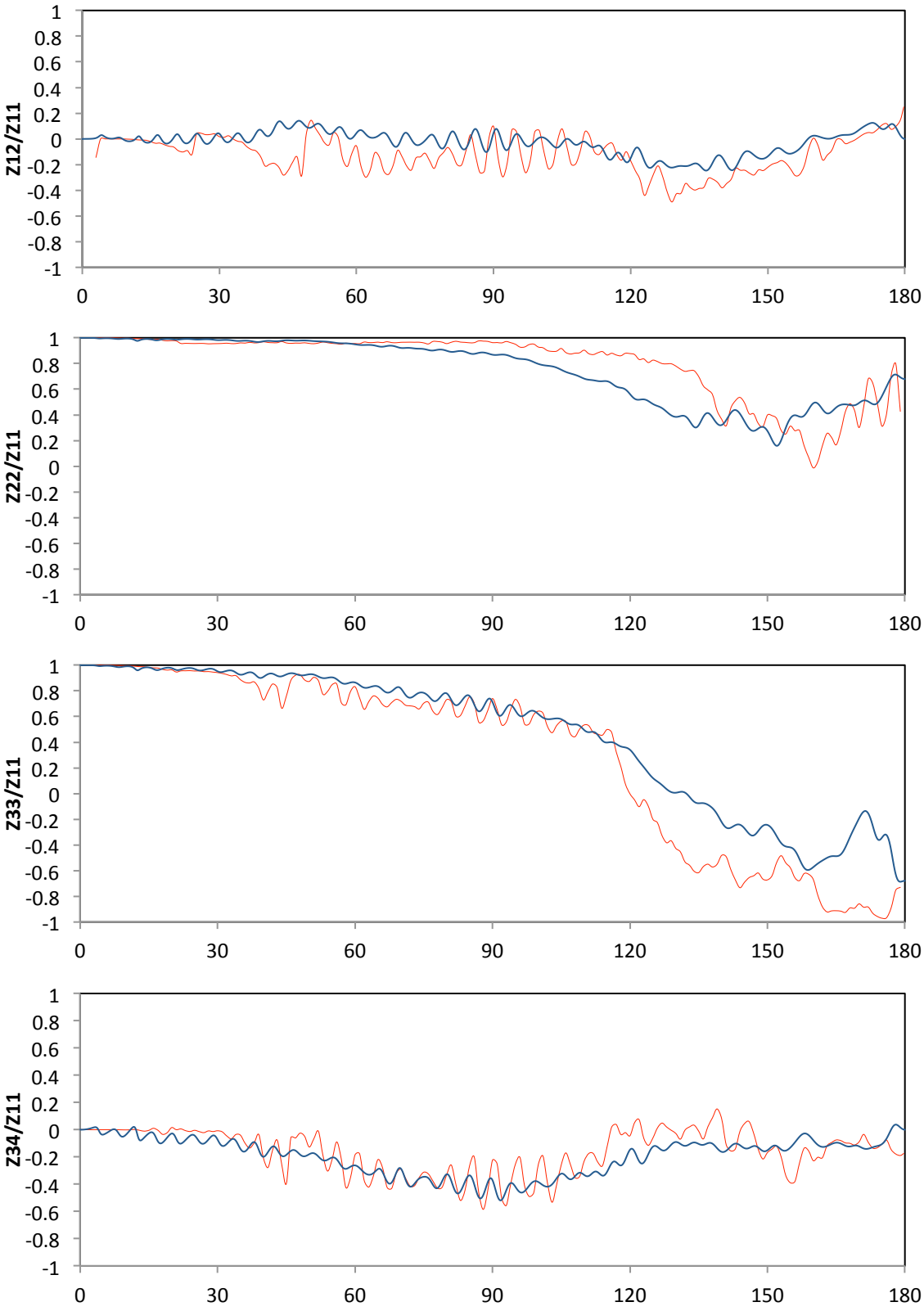
Z12/Z11
Z22/Z11
Z33/Z11
Z34/Z11
1
0.8
0.6
0.4
0.2
0
-0.2
-0.4
-0.6
-0.8
-1
0
30
60
90
120
150
180

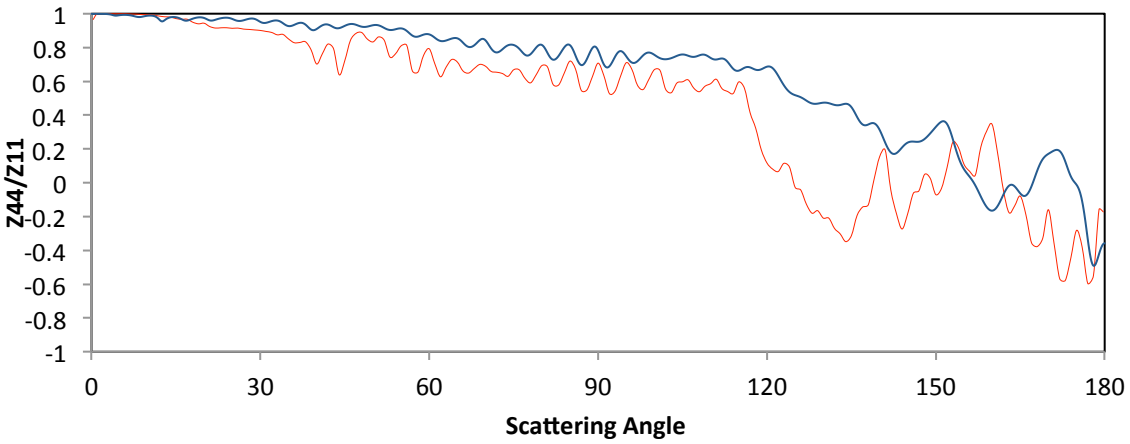

Figure 3 Comparison ADDA - RTMCX: angular distribution of scattering phase matrix elements for randomly oriented hexagonal pure ice crystals with L/D = 1, D = 9.79 μm, λ = 660 nm, refractive index m_{ice} = 1.3117 + i0.0. Blue lines: RTMCX output; green lines: ADDA output. The phase function is expressed in log 2.

Table 1. Comparison of discrete dipole and ray tracing approach for the same pure ice hexagonal prism with random orientation.

	ADDA	RTMCX
Q_{abs}	0.3206	0.426
Q_{ext}	1.298	2
C_{abs}	27.66	44.8
C_{ext}	112.0	206

1.3. BC inclusion model and crystal shapes

We consider a core shell inclusion model, as shown in Figure 4 for an hexagonal ice crystal prism, where a spherical BC core is placed inside the crystal shape and completely contained in it. A large individual sphere mimics a dense aggregate of monomers, whose individual diameters are smaller than the wavelength whereas a smaller sphere may be taken to correspond to an individual monomer. While in reality a sulfate shell deposited on BC monomers decreases their igroscopicity and facilitate their inclusion on ice, for simplicity only the optical properties of ice and BC will be considered. The real (n_r) and imaginary (k_r) refractive indices of BC are expressed according to Flanner et al. (2012) as a function of wavelength (λ, in microns) as:

$$n_r = 2.0248 + 0.1263 \log \lambda + 0.027 \log^2 \lambda + 0.0471 \log^3 \lambda$$
$$k_r = 0.7779 + 0.1213 \log \lambda\, 19 + 0.2309 \log^2 \lambda - 19190.01 \log^3 \lambda \quad (3)$$

in the range 0.3–5.0 μm. The refractive index of ice is set to a constant 1.32 + 0i (Kokhanovsky, 2013) in the range of wavelengths of interest.

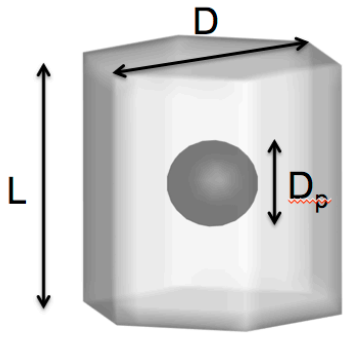

Figure 4 Example of core shell inclusion model.

3. COMPARISON WITH CASPOL MEASUREMENTS

The validation process of the scattering property prediction for ice-carbon compounds is one of the unique features of this work. As we will see, this process is not clear-cut because it is inherently limited by lack of the exact knowledge of both the ice and the BC inclusion morphology. Still, scattering measurements taken under laboratory-controlled conditions provide a unique source of insught. The Cloud and Aerosol Spectrometer with Polarization (CASPOL), manufactured by Droplet Measurement Technologies, is a rather unique measurement tool in that it can measure the optical properties of individual particles. CASPOL was successfully used to evaluate the optical scattering signatures of atmospherically relevant dust particles by Glen and Brooks (2013); the authors then used Scanning Electron Microscopy (SEM) to characterize the shape and morphology of dust samples. More recently, to study the optical properties of ice crystals, CASPOL was placed inside the Continuous Flow Diffusion Chamber (CFDC) (Hiranuma et al., 2013), developed at Texas A&M University: ice crystals were generated by heterogeneous nucleation using mineral dust for ice growth (Glen and Brooks, 2014). In the work reported here, crystals were instead grown on soot particles of different size.

CASPOL features three detectors that operate in the range of particle diameters between 0.6 μm and 50 μm. It collects the light scattered by the target in the forward direction, of intensity FSI, but between the angles of 4° to 12° with respect to the line of sight. Light in the backward direction is detected between 168° and 176°, with the additional polarized detector also in the same range. Labeling the parallel and perpendicular polarization with δ_{par} and δ_{perp}, respectively, the in-situ depolarization ratio (DR) is defined by Glen and Brooks (2013) as

$$\mathrm{DR} = \left(\frac{\delta_{perp}}{\delta_{par}}\right)_{168^\circ \text{ to } 176^\circ}. \quad (4)$$

A number of steps were defined to establish a comparison between our scattering calculations and the CASPOL signals. First, mimicking the spectrometer's signal using either theory or simulation requires the evaluation of the average of the phase function from the Mueller matrix between the angles of 4° and 12°

$$\mathrm{FSI} = \frac{1}{8^\circ}\int_{4^\circ}^{12^\circ} P_{1,1}(\vartheta)\sin(\vartheta)\, d\vartheta, \quad (5)$$

Similarly, for the Mueller-based evaluation of the depolarization ratio:

$$\mathrm{DR} = \frac{1}{8^\circ}\int_{168^\circ}^{176^\circ} \frac{P_{1,1}-2P_{1,2}+P_{2,2}}{P_{1,1}+P_{2,2}}\, d\vartheta. \quad (6)$$

Second, a correspondence between the CASPOL signal and forward scattering needs to be established, as explained in the following. Note that this step is not necessary for the backward polarization intensity since this is constructed as a signal ratio.

1.4. Calibration

CASPOL signal calibration was carried out, as in Glen and Brooks (2013), by generating a monodisperse distribution of spherical particles from a suspension of olive oil and isopropyl alcohol, at wavelength λ = 680 nm. The olive oil test has the obvious advantage that sample shape and orientation effects are not present. The relation between the theoretical diameter calculated for the droplets generated by the Vibrating Orifice Aerosol Generator (VOAG) and the diameter measured by CASPOL was found to be sufficiently close to a 1:1 correspondence.

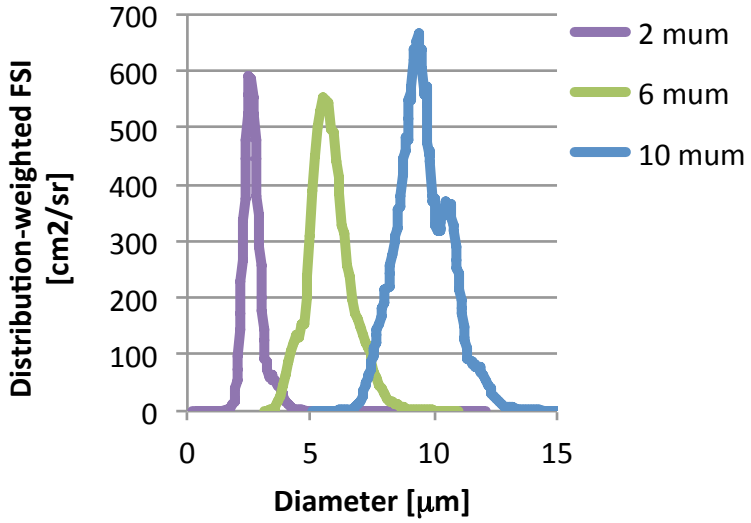

Figure 5. Calculated forward scattering intensity form the three olive oil droplets populations described on Table 2.

Table 2. Parameters of oil droplet lognormal distribution.

	Mean diameter [μm]	Standard deviation [μm]	CASPOL max FSI [a.u.]	Max FSI^{eff} [cm^2/sr]
Set 1	2.6	0.19	3900	591
Set 2	5.7	0.8	4900	556
Set 3	9.4	1.1	6500	665

For each sphere of diameter d_i, the components of the phase matrix can be obtained from the analytical solution to the vector wave equations that describe the scattering behavior of a sphere (Bohren et al., 1983), see Appendix A. Calculations are carried out with the code *bhmie* at λ = 680 nm using a refractive index of 1.46 and the forward scattering intensity is evaluated using Eqn. (2). However, rather than monodisperse, the oil droplet population is better described by a lognormal distribution: Table 2 lists the mean and standard values derived from three different calibration experiments. To calculate the actual forward scattering intensity of one of such populations, we calculate the lognormal probability density function (PDF) with these parameters and take the value w_i to weight the forward scattering distribution of the sphere with diameter d_i:

$$\mathrm{FSI}_i^{eff} = w_i \cdot \mathrm{FSI}_i. \tag{7}$$

The results are shown in Figure 5 for the three sets. The values reported in the last column of Table 2 are the maximum FSI^{eff} for that droplet population. Essentially, the weights from the lognormal function reflect the spread of the signal intensity. For instance, the FSI value for the mean diameter of Set 1 is smaller than the value for the mean diameter of Set 2, However, the population distribution as measured in the calibration experiment is substantially tighter around the mean value, therefore the maximum FSI^{eff} for Set 1 is slightly larger than for Set 2. We claim that such a value can be compared to the CASPOL maximum forward intensity, in arbitrary units, that is listed in the fourth column of Table 2. Thus, by averaging the values of 3900/591, 4900/556 and 6500/665, we conclude that 8.4 signal units approximately correspond to 1 cm^2/sr. This result will be used to analyze the measurements of the main experiment next.

1.5. Measurements with BC-contaminated ice crystals

The procedure to nucleate ice crystals onto soot is briefly explained in the following. A modified Santoro-type laminar diffusion burner (Santoro et al., 1983) was used to generate the soot particles by the incomplete combustion of propane. The soot generator consisted of two concentric tubes; a 66 mm i.d. outer tube with a ceramic laminar flow element on top, which the air went through, and a 7 mm i.d. inner tube which the propane flowed through (Khalizov et al., 2009). The flow rates were ~1.7 L min^{-1} for the airflow, and ~0.75 mL min^{-1} for the propane flow. Typical generated flames extended 7 - 10 cm from the top of the inner tube. An inlet placed approximately 6 cm above the top of the flame directed particles to the CFDC-CASPOL, while, a glass cylinder above the burner acted as a chimney to protect the flame from outside

influences. The soot particles that were used as growth nuclei were either 50, 100, or 200 nm in diameter.

For the ice crystals, an inlet at the top of the CFDC allowed a pre-generated aerosol stream to enter an annular chamber where the sample air is sandwiched between two laminar flows of dry filtered air. The walls of the chamber were coated with ice and held at different temperatures so that a highly controlled supersaturation field could be established between the two walls. As the soot particle traveled through this controlled supersaturation region, it nucleated and formed ice. The resulting ice crystals arriving in the CASPOL ranged in size from 1 to 45 microns; given the generation procedure, we assume that the soot particle was located at approximately the center of each crystal. However, the shape of the crystal, controlled by temperature and supersaturation conditions, is not exactly known. The crystal growth conditions for three experiments are listed in Table 3.

Table 3. Crystal growth conditions

Sample	Soot Diameter	SS Water	SS Ice	Temperature Outer Wall	Temperature Inner Wall	Aerosols Location Temperature
1	50 nm	27.6 %	118 %	-20.6 C	-56.3 C	-55.0 C
2	50 nm	92 %	264 %	-65.0 C	-27.0 C	-41.4 C
3	100 nm	131 %	216 %	-65.0 C	-27.0 C	-38.7 C
4	200 nm	42.0 %	255 %	-65.0 C	-27.0 C	-42.3 C

In the following, we calculate the Mueller matrixes of hexagonal crystal shapes with different aspect ratios (AS) and different sizes of BC insertions as a function of the crystal equivalent diameter,

$$d_E = \left(\frac{6V}{\pi}\right)^{1/3}, \tag{8}$$

where V is the crystal volume. ADDA is used for $d_E < 3$ μm, whereas RTMCX is used for lager diameters.

Figure 6 shows the forward scattering results by using the ratio 8.4:1 that was established in the previous section. Essentially no dependence from the BC size can be identified in the CASPOL measurement, and this behavior is reflected in all our calculations. We note that the CASPOL signal first increases quite sharply until d_E reaches 2 μm, then follows a more moderate increment up to 10 μm, and eventually reaches a plateau. The calculated ADDA and RTMCX forward scattering intensity essentially follow the same trend. It appears that for very small d_E the aspect ratio does not matter substantially, whereas for larger sizes it is crystals with larger aspect ratios (needles) that follow the experimental value better. Assuming the correctness of the calculations, this result would indicate that needle constitute most of the contaminated ice crystals if they are sufficiently large.

The measured backscattering polarization intensity, shown from Figure 7 to Figure 9, exhibits a different behavior with respect to forward scattering in that a dependence from the BC size can be detected. For samples 1 and 2, it would appear that crystal growth conditions are also, as the

BSI values from the two sets are quite different while the nominal BC size is kept at 50 nm. Comparison with simulation results requires the evaluation of Eqn. (3) and therefore no scaling is necessary. While agreement is not perfect, a qualitative behavior similar to the one displayed by the CASPOL measurements can be observed. Interestingly, the two 50 nm cases are matched more closely by AR = 0.5 crystals (plates) than by larger aspect ratios, whereas these same shapes consistently under-predict the polarization ratio in the other two samples. There is not a substantial difference for AR > 1.

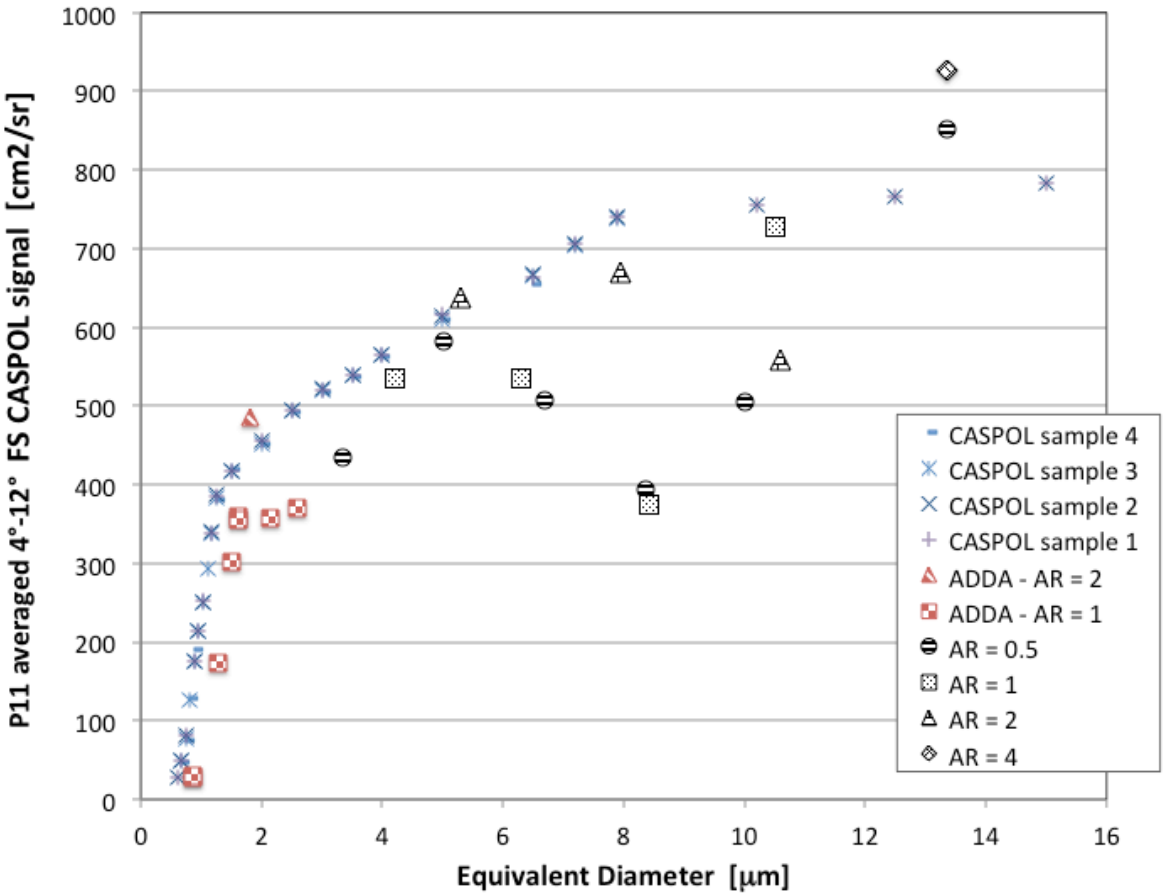

Figure 6. Forward scattering: the CASPOL signal is compared to simulation results from ADDA (red patterned) and RTMCX (black patterned).

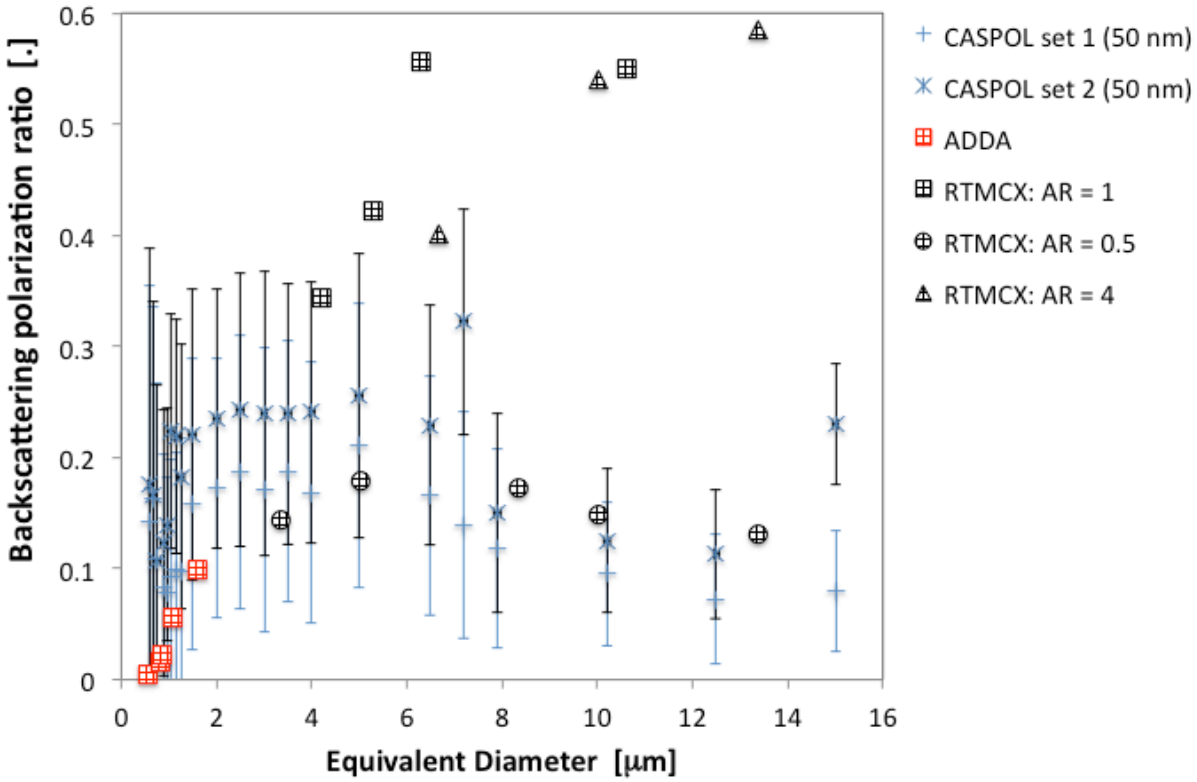

Figure 7. Back-scattering polarization ratio at 50 nm.

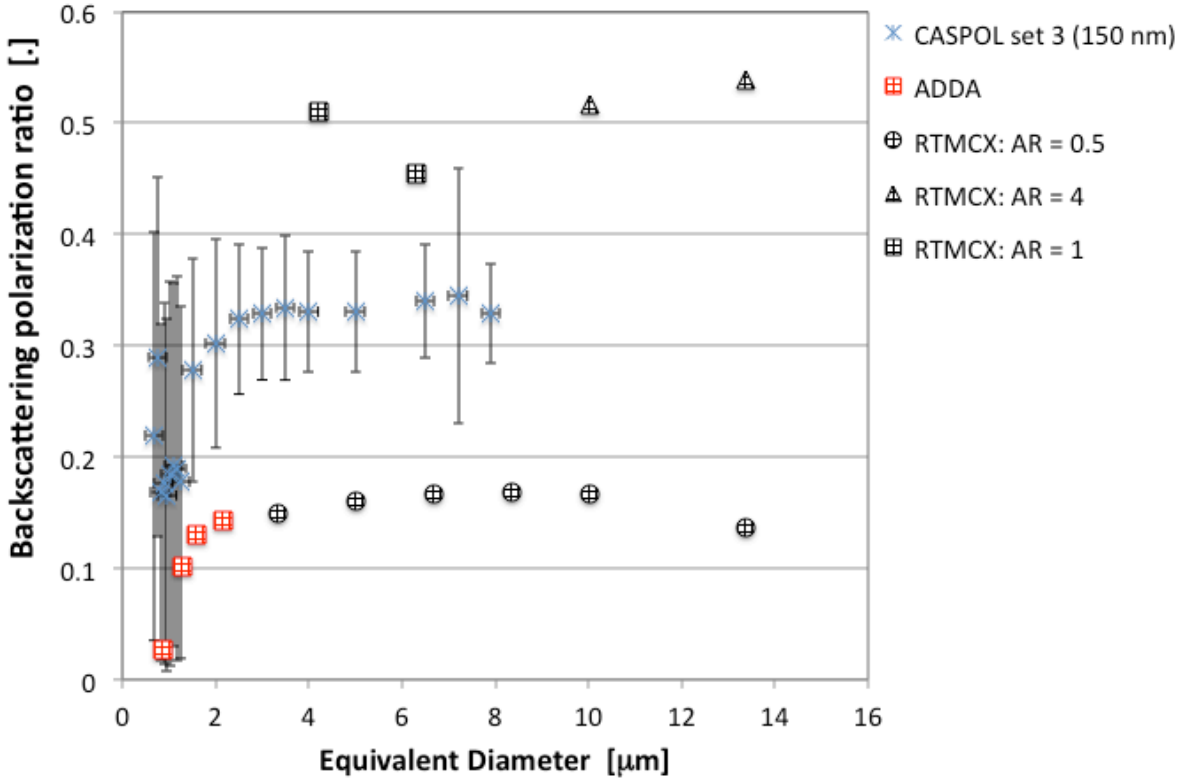

Figure 8. Back-scattering polarization ratio at 100 nm.

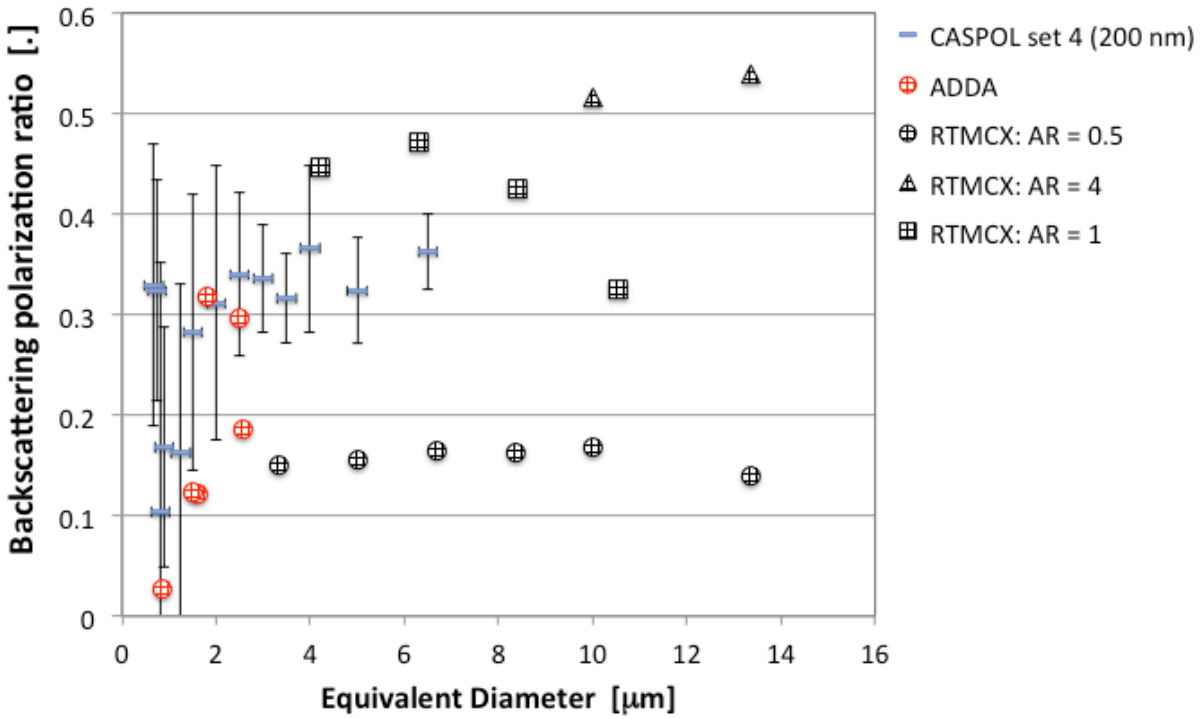

Figure 9. Back-scattering polarization ratio at 200 nm.

4. RESULTS AND DISCUSSION

It is well known that the internal mixing state of soot and ice corresponds to substantially more absorbed radiation compared with its external mixing counterpart because of light absorption enhancement from all directions (e.g., Liou et al. 2013). The soot absorption effect is largely confined to wavelengths shorter than about 1.4 mm, beyond which ice absorption predominates. Liou et al. (2013) studied the effect of internal and external mixings of BC in ice particles on the radiative properties of contrail cirrus using a simple ice plate model. A parameter not investigated in that study was the effect of the position of the BC inclusion inside the crystal relative to the shape of the crystal.

1.6. Hexagonal crystal with centered inclusion

As an illustrative example of the effect of BC inclusion, a hexagonal crystal with aspect L/D = 1 is considered: D = 9.79 μm, D_p = 6.15 μm, λ = 660 nm. The size parameter for this simulation is X = 2πD/λ = 500, which is sufficiently large for the geometrical optics approximation to be valid (Liou, 2002).

Figure 10 shows the angular variation of the scattering phase matrix from RTMCX with (blue lines) and without (red lines) the inclusion placed at the center of the prism. Also shown for reference is the case of the same BC sphere in an infinite ice medium (green lines). The plots indicate that the presence of a strongly absorbing inclusion shifts the scattering characteristics of

the compound particle towards that of a sphere ($Z_{11} \approx Z_{22}$, $Z_{33} \approx Z_{44}$, $Z_{34} = -Z_{43} \approx 0$). The halo peaks of the hexagonal prism crystal are still present, but their magnitudes are significantly smaller with the BC inclusion. The angular distributions of Z_{34} and Z_{43} of the compound particle do not show specific characteristics of either BC sphere or pure crystal and appear to combine both characteristics in a nonlinear fashion. The absorption efficiency increases from 0 for the pure crystal to 0.44 for the compound particle; the asymmetry factor and scattering albedo drop from 0.93 and 1 for the pure crystal to 0.81 and 0.78 for the compound particle, respectively.

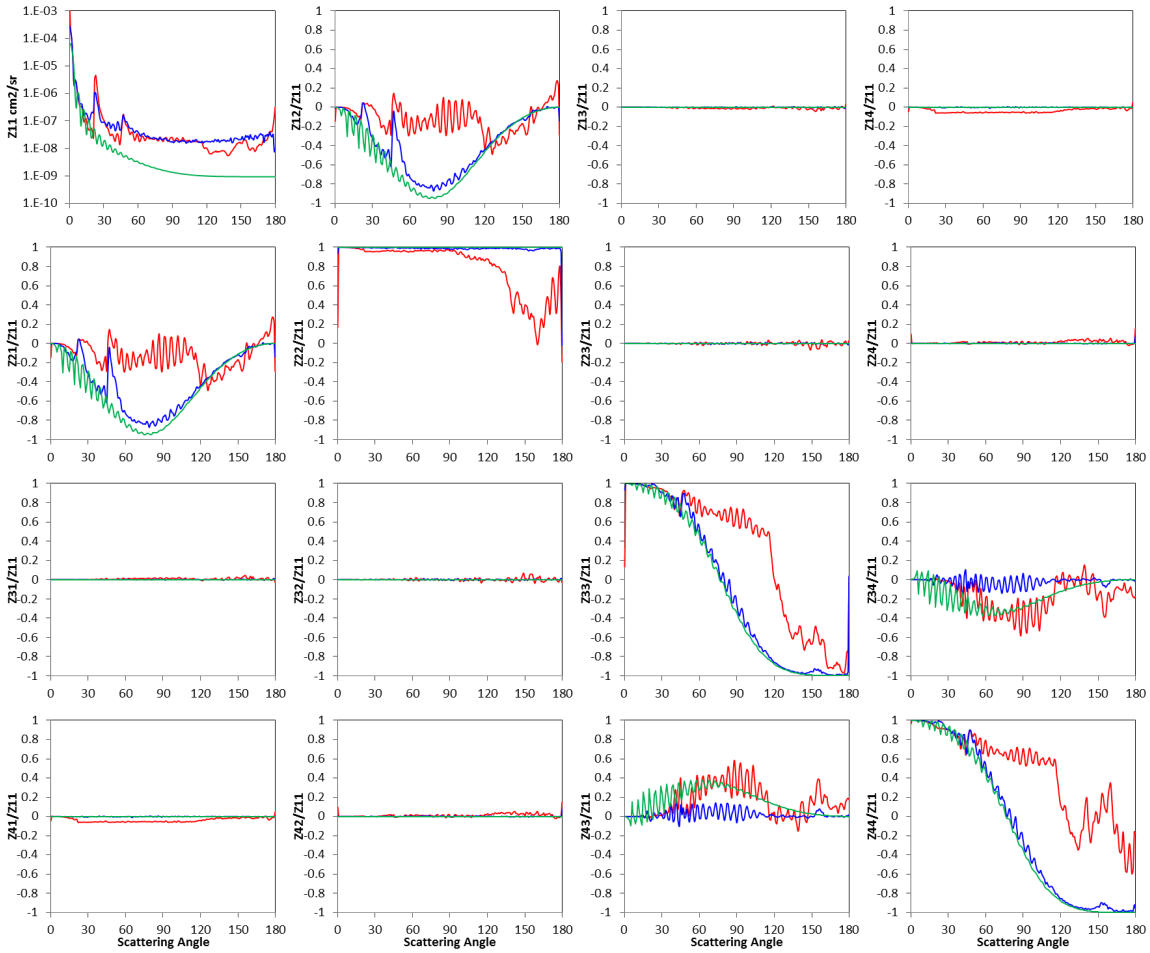

Figure 10. Angular distribution of scattering phase matrix elements for randomly oriented hexagonal ice crystals with a BC inclusion in the center: L/D = 1, D = 9.79 μm, D_p = 6.15 μm, λ = 660 nm, refractive index m_{ice} = 1.3117 + i0.0, m_{BC} = 1.54 + i0.37. The RTMCX simulations use 10^4 orientations with 10^3 incident rays per orientation. Blue lines: 20% volume BC; red lines: pure crystal; green lines: BC sphere inside infinite ice medium.

We now examine more closely the effect of soot volume fraction on the cross-section magnification, the ratio between the absorption cross-section of the BC-ice compound and the absorption cross-section of the BC sphere in air. The latter value is C_{abs} = 30.3 μm^2 (35.71) at λ = 0.660 μm (the absorption cross section of the pure ice crystal is taken to be zero). The results

from a set of RTMCX calculations are shown in Figure 11. Using the same crystal shape and centered black carbon sphere of the previous example, the hexagonal prism diameter is varied from 9.79 μm to 195 μm, corresponding to the decrease in BC volume fraction shown in Figure 11a. The same information is displayed in Figure 11b by taking the minimum distance between the sphere surface and the hexagonal prism surface, normalized by wavelength, d/λ. We see that the absorption of the compound particle increases by about 75% when the BC sphere is embedded in the crystal, confirming findings reported by Flanner et al. (2012) and references therein; the increase is also independent from the actual volume fraction as long as this is sufficiently small (less than 5% in this case). Looking at in Figure 11b, another way to state this result is that the cross-section magnification remains the same if the embedded BC is sufficiently removed from the crystal's surfaces.

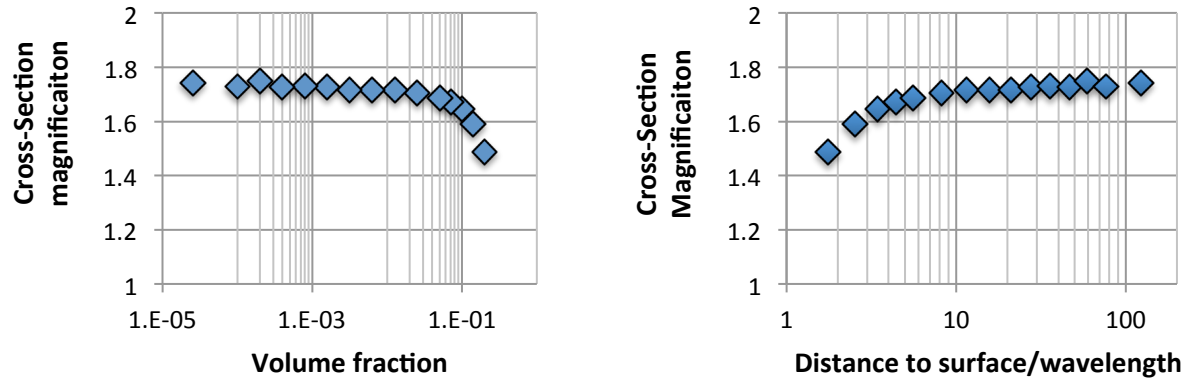

(a) (b)

Figure 11. Magnification of the absorption cross-section of a compound particle with fixed BC location and diameter but varying crystal volume. (a) magnification vs. BC volume fraction; (b) magnification vs. smallest distance between centered sphere and crystal surface.

The decrease in cross-section magnification noted in the previous plots is now re-examined by parameterizing the inclusion position while keeping constant the size of the crystal (D = L = 97.9 μm) and of the inclusion (D_p = 6.15 μm). This is illustrated in Figure 12 where the absorption cross-section of the compound particle is again plotted as a function of the normalized distance to the crystal surface, corresponding to different values of the BC sphere center along the crystal's z-axis. This time we also report in the form of uncertainty interval the 95% confidence interval, that is, the standard deviation from five RTMCX calculation multiplied by the t-factor 2.57. In this case too we find that the absorption cross-section of the compound particle is larger than the C_{abs} of same BC in air, with a magnification factor around the value 1.7, and that the magnification decreases when the gap between the BC sphere and the crystal face is less than 10 λ.

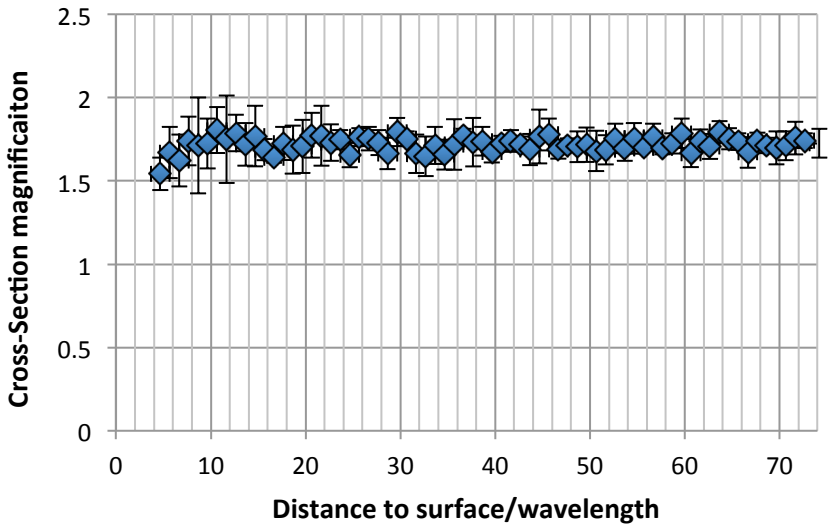

Figure 12. Absorption cross-section vs. BC distance from the crystal surfaces. Error bars represent 95% confidence intervals derived from 5 RTMCX calculations (100 orientations with 100 rays per orientation).

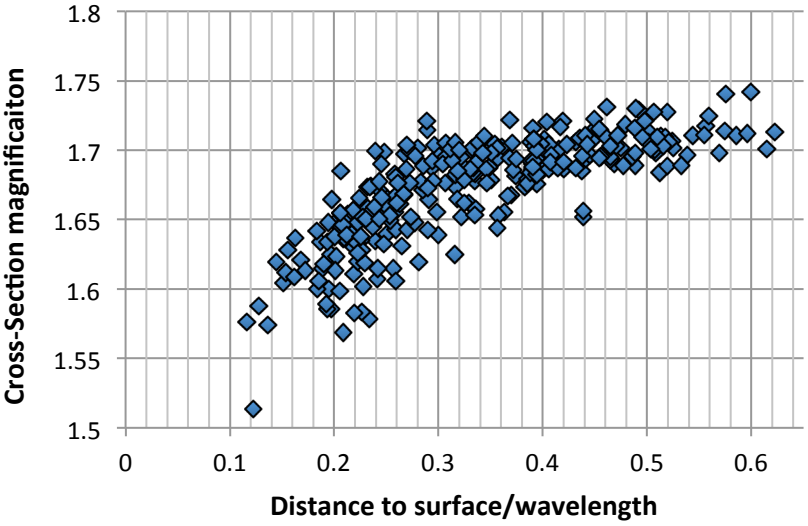

Figure 13. Cross-section magnification effect from 300 ADDA sample calculations parameterized by the position of the BC insertion.

Our ray tracing calculations are intrinsically limited in the minimum distance the inclusion can be placed with respect to the external surfaces of the scatterer. The ADDA approach then provides a completing view of the magnification effect when the distance of the BC particle is comparable or smaller than the wavelength. In Figure 13, the BC inclusion is allowed to take any position inside the crystal, as long as the sphere is completely contained inside the crystal, for a total of 300 independent samples. In this set of calculations, D = L = 0.8508 μm (the relatively small size parameter enables many calculations in a short period of time) and the BC diameter is 0.21 μm. As in the rest of this work, the variation due to the discretization of the spherical shape

with cubic dipoles is kept small, in this case around 1.4% of the sphere volume. The maximum available distance to the crystal surface is $d/\lambda = \sqrt{3}/4 \cdot D/\lambda = 0.692$ with $\lambda = 0.532$ μm. The points resulting from the sampling are distributed in a broader cloud that becomes more disperse when the inclusion becomes closer to one of the crystal surfaces. There absorption cross-section magnification decreases to a value slightly above 1.5 in the limit case of the monomer almost touching the crystal surface. For more centered locations, the magnification is again close to 1.7. This is quite a remarkable result since it is obtained using a crystal shape and BC insertion that are two orders of magnitude smaller than in the previous example.

1.7. Effects due to the crystal's shape

We can now begin to differentiate the observations above based on the crystal's shape. The previous results would suggest that crystals with larger surface area (for a given volume of ice) are less efficient in enhancing the absorption efficiency because a larger percentage of the inclusions could end up being closer to the crystal surface. As shown next, this effect may, however, be offset by a higher efficiency of intercepting a beam of light and channeling it to an absorbing particle. It has been previously shown that the variation of the asymmetry factor versus the aspect ratio presents a distinctive "V-pattern" (Neshyba *et al.* 2003; Grenfell *et al.* 2005; Fu 2007) with the minimum near the unit aspect ratio. For pure crystals, Yang and Fu (2009) systematically analyzed the effect of aspect ratio on the asymmetry parameter and attributed it to the collimated rays that transmit through two parallel faces and propagate along the incident direction.

The previous exercise is continued by considering different aspect ratios to represent a range of shape variations in ADDA. Figure 14 is a scatter plot of the absorption and scattering coefficients for four AR values (0.3, 1, 3, 4 and 5), each with 300 realizations of the BC position generated by a random uniform distribution. The points are colored by the closest distance from the prism sides, normalized by the wavelength (here, $\lambda = 532$ nm). Within the variation due to the inclusion position, the absorption coefficient increases more substantially when AR = 5 and 4, followed by AR = 0.3, 3, and finally 1. We note that since the crystal volume is maintained constant, the maximum d value that can be obtained between the inclusion and the crystal faces occurs when L = D. In terms of scattering, the coefficient increases as the aspect ratio decreases, with a rather small variation due to the position of the inclusion inside the crystal within each values of AR. The absorption coefficient exhibits a larger excursion, approximately 7-12%, and as previously observed it increases from the smallest to the largest possible distance to the prism sides.

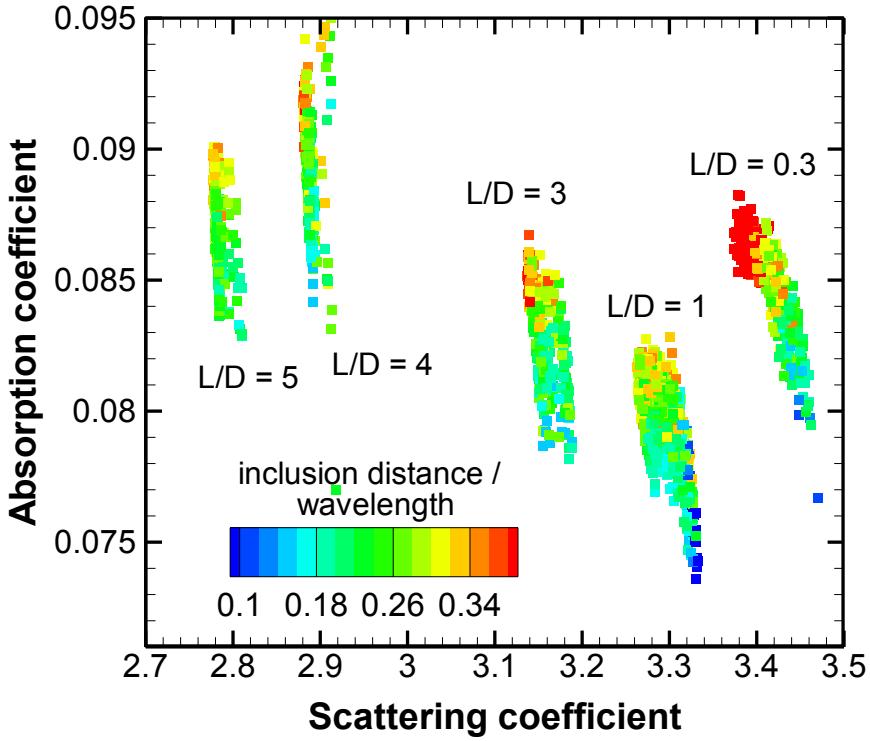

Figure 14. Absorption coefficients vs. scattering coefficients: a single BC sphere (of 0.21 μm in diameter) is located at random locations (300 in total) inside a small hexagonal prism of ice with volume 0.4 μm^3. Symbols are colored according to the minimum distance between the center of the BC inclusion and the sides of the ice crystal, normalized by wavelength.

To conclude this section, the absorption magnification study is extended in **Error! Reference source not found.** by using either ray-tracing or discrete dipole approximation (depending on applicable range). The incident light wavelength is 0.660 μm. The range of BC volume fraction is between 4 10^{-7} and 2 10^{-2}. The BC inclusion is always located in the center of the crystal; depending on its diameter, it can be interpreted as either a single monomer or a compact aggregate. In the ADDA calculations (full symbols), D_p = 0.1 μm; the volume of the L=D hexagonal prism is 0.1 μm^3 and different aspect ratios are obtained by increasing or decreasing L while keeping fixed D. Thus, the normalized distance of the insertion center to the cristal faces is a fraction of 1. In the RTMCX calculations (empty symbols) D_p = 6.16 μm and $d/\lambda > 10$. Besides hexagonal prisms, randomly generated individual Voronoi shells (Figure 1) and their aggregates are also considered. Aggregates are organized in more elongated crystals (square symbols in **Error! Reference source not found.**) or in shapes that are closer to spherical (lozenges).

As before, the absorption cross-section values of **Error! Reference source not found.** are normalized by the corresponding cross-section of the BC sphere in air. All the data points indicate that the magnification is substantial, of the order of 60% or more. This effect appears to be independent from the volume fraction of the BC inclusion, as pointed out previously;

moreover, within each data set the difference in magnification appear to depend on the shape. Particularly, individual Voronoi cells, near-spherical aggregates and hexagonal prisms with AR close to unity show a magnification of 1.7, whereas elongated aggregates and prisms have a larger absorption cross-section of two or larger. In the set of hexagonal prisms, the rod-like and plate-like shapes display the largest increase in cross-section, with AR = 10 reaching 2.2; the L=D shape has the lowest. In most of these cases, $d/\lambda > 10$. Interestingly, the trend of larger magnification ratio for elongated crystals is reversed if the characteristic lengths are sub-micron, because $d/\lambda = 0.35$: the magnification is the largest for L = 1, 2, 5D, which offer the greatest possible distance d/λ, but it decreases for L = 0.7D, 0.4D and 0.3D because d/λ becomes smaller.

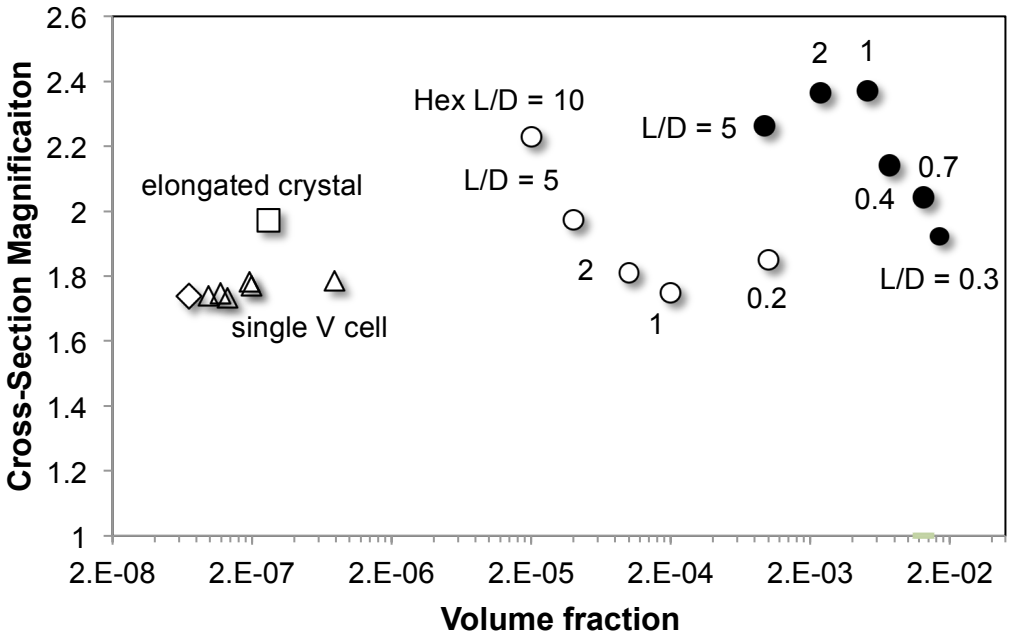

Figure 15. Cross-section magnification of absorption vs. BC volume fraction for different aspect ratios and parameter sizes. See text for explanation.

5. CONCLUSIONS

In this paper, the discrete dipole and ray tracing methodologies have been tested for compound ice-soot particles. These two techniques were chosen for as the best compromise between accuracy and flexibility in particle representation over the broadest parameter size. Of particular interest is the presentation of new scattering data, forward intensity and backward polarized intensity, of such BC-seeded particles as obtained under controlled temperature and flow conditions in the Continuous Flow Diffusion Chamber built at Texas A&M University. For instance, it is found that the polarization intensity is somewhat sensitive to the size of the BC inclusion and possibly on details of the crystal preparation. Computationally, a complete validation of the numerical techniques employed in this work is still beyond our capability

because of the lack of complete information about the morphology of the compound particles. However, we find the qualitative agreement with the data to be encouraging.

Literature results have suggested that the shape of the ice crystal, the concentration of BC and the distribution of the monomers have a combined effect on the optical properties. We show that

- Absorption enhancement is independent from BC content as long as this is sufficiently small, in percentages that are easily found in atmospheric ice.
- The enhancement is practically independent from the position of the BC inclusion, as long as this is sufficiently removed from the crystal's surfaces. In this case, very elongated or plate-like crystals achieve the greatest cross-section magnification.
- If the ice crystal is very small compared to wavelength, then the BC volume fraction is larger and can affect directly the absorption magnification. The dependence on the crystal aspect ratio also tends to be reversed, since the particles that are closest to a spherical shape are also the ones with the largest available distance from its surfaces.

6. REFERENCES

Ayrancı, I., R. Vaillon, and N. Selçuk, 2007: Performance of discrete dipole approximation for prediction of amplitude and phase of electromagnetic scattering by particles. *Journal of Quantitative Spectroscopy and Radiative Transfer*, **103,** 83-101.

Bailey, M. P., and J. Hallett, 2009: A comprehensive habit diagram for atmospheric ice crystals: Confirmation from the laboratory, AIRS II, and other field studies. *Journal of the Atmospheric Sciences*, **66,** 2888-2899.

Bi, L., P. Yang, G. W. Kattawar, and M. I. Mishchenko, 2013. Efficient implementation of the invariant imbedding T-matrix method and the separation of variables method applied to large nonspherical inhomogeneous particles. *Journal of Quantitative Spectroscopy and Radiative Transfer*.

Bi, L. and P. Yang, 2014: Accurate simulation of the optical properties of Atmospheric ice crystals with the invariant imbedding T-matrix method. *Journal of Quantitative Spectroscopy and Radiative Transfer*.

Bi, L., P. Yang, C. Liu, B. Yi, B. A. Baum, B. van Diedenhoven, H. Iwabuchi, 2014: Assessment of the accuracy of the conventional ray-tracing technique: Implications in remote sensing and radiative transfer involving ice clouds. *Journal of Quantitative Spectroscopy & Radiative Transfer* **146** 158–174

Bohren, C. F., Huffman, D. R. 1983: Absorption and Scattering of Light by Small Particles, John Wiley & Sons.

Bond, T., and Bergstrom, 2006: Light absorption by carbonaceous particles: an investigative Review. *Aerosol Science and Technology,* 40:27–67.

Bond, T., and Coauthors, 2013: Bounding the role of black carbon in the climate system: A scientific assessment. *Journal of Geophysical Research: Atmospheres*.

Cappa, C. D., and Coauthors, 2012: Radiative absorption enhancements due to the mixing state of atmospheric black carbon. *Science*, **337,** 1078-1081.

Chen, H., M. Iskander, and J. Penner, 1990: Light scattering and absorption by fractal agglomerates and coagulations of smoke aerosols. *Journal of Modern Optics*, **37,** 171-181.

Chýlek, P., Videen, G., Geldart, D., Dobbie, J. S., and Tso, H., 2000: Effective medium approximations for heterogeneous particles. *Light Scattering by Nonspherical Particles: Theory, Measurements, and Applications*, **1,** 274.

Danielsen, R. E., Moore, D. R., and van de Hulst, H. C., 1969: The transfer of visible radiation through clouds, *J. Atmos. Sci.*, **26**, 1078-1087.

Davis, P. J., and P. Rabinowitz, 2007: *Methods of numerical integration.* Courier Dover Publications.

Della Sala, F., and S. D'Agostino, 2013: *Handbook of Molecular Plasmonics.* CRC Press.

Draine, B. T., 1988: The discrete-dipole approximation and its application to interstellar graphite grains. *The Astrophysical Journal*, **333,** 848-872.

——, 2000: The discrete dipole approximation for light scattering by irregular targets. *Light Scattering by Nonspherical Particles: Theory, Measurements, and Applications*, **1,** 131.

Draine, B. T., and J. Goodman, 1993: Beyond Clausius-Mossotti-Wave propagation on a polarizable point lattice and the discrete dipole approximation. *The Astrophysical Journal*, **405,** 685-697.

Flanner, M., X. Liu, C. Zhou, J. E. Penner, and C. Jiao, 2012: Enhanced solar energy absorption by internally-mixed black carbon in snow grains. *Atmospheric Chemistry and Physics*, **12,** 4699-4721.

Flatau, P. J., and B. Draine, 1994: Discrete-dipole approximation for scattering calculations. *J. Opt. Soc. Am. A*, **11,** 1491.

Fu, Q., 2007: A new parameterization of an asymmetry factor of cirrus clouds for climate models. *Journal of the Atmospheric Sciences*, **64,** 4140-4150.

Fuller, K. A.,1995: Scattering and absorption cross sections of compounded s

pheres, III, Spheres containing arbitrarily located spherical inhomogeneities, *J. Opt. Soc. Am. A*, **12,** 893-904.

Garnett, J. M., 1906: Colours in metal glasses, in metallic films, and in metallic solutions. II. *Philosophical Transactions of the Royal Society of London. Series A, Containing Papers of a Mathematical or Physical Character***,** 237-288.

Ghan, S. J., and S. E. Schwartz, 2007: Aerosol properties and processes: A path from field and laboratory measurements to global climate models. *Bulletin of the American Meteorological Society*, **88,** 1059-1083.

Glen A. and Brooks, S. D., 2013: A new method for measuring optical scattering properties of atmospherically relevant dusts using the Cloud and Aerosol Spectrometer with Polarization (CASPOL). *Atmos. Chem. Phys.*, **13**, 1–12.

Glen A. and Brooks, S. D., 2014, Single particle measurements of the optical properties of small ice crystals and heterogeneous ice nuclei Aerosol Science and Technology **48**(11), 1123-1132.

Grenfell, T. C., S. P. Neshyba, and S. G. Warren, 2005: Representation of a nonspherical ice particle by a collection of independent spheres for scattering and absorption of radiation: 3. Hollow columns and plates. *Journal of Geophysical Research: Atmospheres (1984–2012)*, **110**.

Heymsfield, A. J., and J. Iaquinta, 2000: Cirrus crystal terminal velocities. *Journal of the Atmospheric Sciences*, **57,** 916-938.

Hiranuma, N., S. D. Brooks, R. C. Moffet, A. Glen, A. Laskin, M. K. Gilles, P. Liu, A. M. Macdonald, J. W. Strapp, and G. M. McFarquhar (2013), Chemical characterization of individual particles and residuals of cloud droplets and ice crystals collected on board research aircraft in the ISDAC 2008 study, *Journal of Geophysical Research-Atmospheres*, **118**(12), 6564-6579.

Ishimoto, H., K. Masuda, Y. Mano, N. Orikasa, A. Uchiyama, 2012: Irregularly shaped ice aggregates in optical modeling of convectively generated ice clouds, *Journal of Quantitative Spectroscopy & Radiative Transfer* **113** 632-643.

Kahnert, M., T. Nousiainen, and H. Lindqvist, 2013: Models for integrated and differential scattering optical properties of encapsulated light absorbing carbon aggregates. *Optics express*, **21,** 7974-7993.

Kaufman, Y., and Coauthors, 1994: Size distribution and scattering phase function of aerosol particles retrieved from sky brightness measurements. *Journal of Geophysical Research: Atmospheres (1984–2012)*, **99,** 10341-10356.

Kinne, S., and Coauthors, 1997: Cirrus cloud radiative and microphysical properties from ground observations and in situ measurements during FIRE 1991 and their application to exhibit problems in cirrus solar radiative transfer modeling. *Journal of the atmospheric sciences*, **54,** 2320-2344.

Kokhanovsky, A. A., 2013: *Light Scattering Reviews 8: Radiative transfer and light scattering.* Springer Science & Business.

Korolev, A., G. Isaac, and J. Hallett, 1999: Ice particle habits in Arctic clouds. *Geophysical research letters*, **26,** 1299-1302.

Lahaye, J., and F. Ehrburger-Dolle, 1994: Mechanisms of carbon black formation. Correlation with the morphology of aggregates. *Carbon*, **32,** 1319-1324.

Lee, Y.-K., and Coauthors, 2003: Use of circular cylinders as surrogates for hexagonal pristine ice crystals in scattering calculations at infrared wavelengths. *Applied optics*, **42,** 2653-2664.

Liou, K.-N. 2002:*"An Introduction to Atmospheric Radiation"*, 2nded, Academic Press

Liou, K.-N., 1986: Influence of cirrus clouds on weather and climate processes: A global perspective. *Monthly Weather Review*, **114,** 1167-1199.

Liou, K.-N., Takano, Y. and Yang, P., 2011: Light absorption and scattering by aggregates: Application to black carbon and snow grains. *Journal of Quantitative Spectroscopy and Radiative Transfer*, **112,** 1581-1594.

Liou, K.-N., Takano, Y., Yue, Q., and Yang, P., 2013: On the radiative forcing of contrail cirrus contaminated by black carbon. *Geophysical Research Letters*, **40,** 778-784.

Liu, L., and M. I. Mishchenko, 2007: Scattering and radiative properties of complex soot and soot-containing aggregate particles. *Journal of Quantitative Spectroscopy and Radiative Transfer*, **106,** 262-273.

Macke, A., P. N. Francis, G. M. McFarquhar, and S. Kinne, 1998: The role of ice particle shapes and size distributions in the single scattering properties of cirrus clouds. *Journal of the atmospheric sciences*, **55,** 2874-2883.

McFarquhar, G. M. and Coauthors, 2007: Ice properties of single-layer stratocumulus during the Mixed-Phase Arctic Cloud Experiment: 1. Observations. *Journal of Geophysical Research*, **112**, D24201.

Mikhailov, E., S. Vlasenko, and A. Kiselev, 2001: Optics and structure of carbonaceous soot aggregates. *Optics of Nanostructured Materials***,** 413-466.

Mishchenko, M. I., and K. Sassen, 1998: Depolarization of lidar returns by small ice crystals: An application to contrails. *Geophysical Research Letters*, **25,** 309-312.

Mishchenko, M. I., and Macke, M. 1999: How big should hexagonal ice crystals be to produce halos? *Appl. Opt.* **38**:1626-9.

Mitchell, D. L., 2002: Effective Diameter in Radiation Transfer: General Definition, Applications, and Limitations. *Journal of the Atmospheric Sciences*, **59**, 2330-2346.

Muinonen, K., Nouisiainen, T., Lindqvist, H., Muñoz, O., Videen, G. 2009: Light scattering by Gaussian particles with internal inclusions and roughened surfaces using ray optics. *Journal of Quantitative Spectroscopy & Radiative Transfer* **110**, 1628–1639.

Neshyba, S. P., T. C. Grenfell, and S. G. Warren, 2003: Representation of a nonspherical ice particle by a collection of independent spheres for scattering and absorption of radiation: 2. Hexagonal columns and plates. *Journal of geophysical research*, **108,** 4448.

Nicolet, M., M. Schnaiter, and O. Stetzer, 2012: Circular depolarization ratios of single water droplets and finite ice circular cylinders: a modeling study. *Atmospheric Chemistry and Physics*, **12,** 4207-4214.

Nousiainen T, Muinonen K, Avelin J, Sihvola A., 2001: Microwave backscattering by nonspherical ice particles at 5.6 GHz using second-order perturbation series. *Journal of Quantitative Spectroscopy Radiation Transfer*, **70**, 639-61.

Nousiainen, T., 2009. Optical modeling of mineral dust particles: A review. *Journal of Quantitative Spectroscopy and Radiative Transfer*, **110,** 1261-1279.

Penttilä, A., and Coauthors, 2007: Comparison between discrete dipole implementations and exact techniques. *Journal of Quantitative Spectroscopy and Radiative Transfer*, **106,** 417-436.

Penttilä, A. and K. Lumme, 2011: Optimal cubature on the sphere and other orientation averaging schemes, J. Quant. Spectrosc. Radiat. Transfer 112, 1741-1746 (2011).

Piller, N. B., 1999: Coupled-dipole approximation for high permittivity materials. *Optics communications*, **160,** 10-14.

Purcell, E. M., and C. R. Pennypacker, 1973: Scattering and absorption of light by nonspherical dielectric grains. *The Astrophysical Journal*, **186,** 705-714.

Ramanathan, V. and G. Carmichael, 2008: Global and regional climate changes due to black carbon. *Nature geoscience*, **1,** 221-227.

Santoro, R., H. Semerjian, and R. Dobbins (1983), Soot particle measurements in diffusion flames, *Combust. Flame*, **51**, 203-218.

Schmitt, C. G. and A. J.Heymsfield, 2010: The Dimensional Characteristics of Ice Crystal Aggregates from Fractal Geometry. J. Atmos. Sci., **67,** 1605-1616.

Schwarz, J., and Coauthors, 2006: Single-particle measurements of midlatitude black carbon and light-scattering aerosols from the boundary layer to the lower stratosphere. *Journal of Geophysical Research: Atmospheres (1984–2012)*, **111**.

Sorensen, C., 2001: Light scattering by fractal aggregates: a review. *Aerosol Science & Technology*, **35,** 648-687.

Videen, G., and P. Chýlek, 1998: Scattering by a composite sphere with an absorbing inclusion and effective medium approximations. *Optics communications*, **158,** 1-6.

Yang, P., and Q. Fu, 2009: Dependence of ice crystal optical properties on particle aspect ratio. *Journal of Quantitative Spectroscopy and Radiative Transfer*, **110,** 1604-1614.

Yang, P., L. Bi, B. A. Baum, K.-N. Liou, G. W. Kattawar, M. I. Mishchenko, and B. Cole, 2013: Spectrally Consistent Scattering, Absorption, and Polarization Properties of Atmospheric Ice Crystals at Wavelengths from 0.2 to 100 μ m. *Journal of the Atmospheric Sciences*, **70,** 330-347.

Yurkin, M. A., and A. G. Hoekstra, 2007: The discrete dipole approximation: an overview and recent developments. *Journal of Quantitative Spectroscopy and Radiative Transfer*, **106,** 558-589.

——, 2013: User manual for the discrete dipole approximation code ADDA 1.2.

Yurkin, M. A., V. P. Maltsev, and A. G. Hoekstra, 2007: The discrete dipole approximation for simulation of light scattering by particles much larger than the wavelength. *Journal of Quantitative Spectroscopy and Radiative Transfer*, **106,** 546-557.

APPENDIX A: MIE SCATTERING CALCULATION

The reason for discussing the Mie scattering in the context of scattering properties of ice crystals with inorganic inclusions is twofold: on one hand it is used to illustrate the complex angular distribution of scattered light for perfectly shaped, homogeneous particles that are large compared with the wavelength of the incident light. On the other hand, Mie theory will be used to describe the scattering and absorption properties of the particles suspended in the crystal. These particles exhibit, for the spectral region of atmospheric radiation, sizes similar to or smaller than the wavelength of the internal electromagnetic wave. For strongly absorbing inclusions, such as soot agglomerates, extinction is dominated by absorption in this size range, or, in other words, scattering characteristics play a minor role (Bohren *et al.* 1983), which justifies approximation of complex particle shapes through spheres. We exploit this in simulations of the scattering properties of ice crystals with black carbon inclusions located at fixed positions inside the crystal using with a Monte-Carlo ray-tracing software (see below).
Mie scattering commonly refers to the angular distribution of electromagnetic radiation scattered by a homogeneous, isotropic sphere of any size illuminated by a planar electromagnetic wave. The derivations of the analytical solution to the vector wave equations that describe the scattering behavior of a sphere are readily available in the literature (e.g. Bohren *et al.* 1983, van de Hulst 1957, Kerker 1969).

A.1. Results for non-absorbing spheres

Points to make: (1) Ripple structure in all but the smallest sizes (see also Bohren *et al.* 1983, for surface modes), (2) scattering intensities decrease with increasing scattering angle (light is scattered predominately in forward direction), with exception of peak around 135° (rainbow angle) (3) observation of ripple structure requires high angular resolution (4) perfectly shaped, smooth, homogeneous non-absorbing spheres cause highly oscillatory angular distribution patterns even when particles diameters that are moderately larger than wavelength (size parameter 10 corresponds to D/L ~ 3.2).

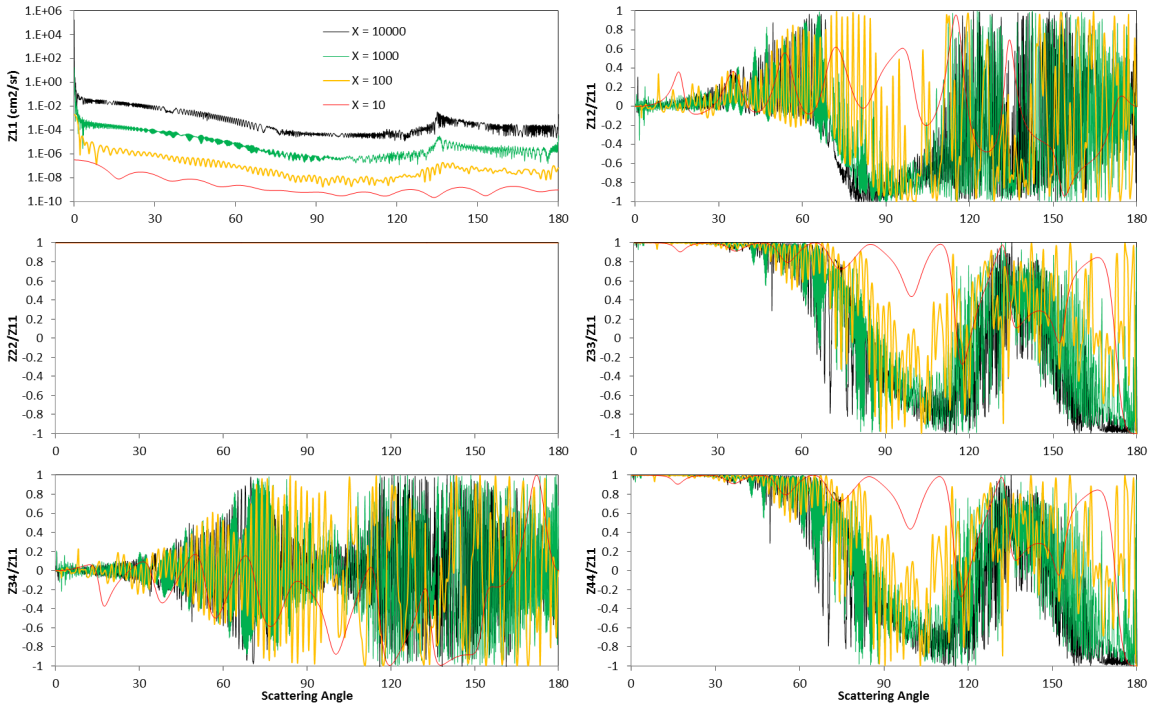

Figure 16 Angular distribution of scattering phase matrices for spheres with size parameters *X* = 10, 100, 1000, and 10000. The angular resolution is 0.1°. For spheres Z_{13}, Z_{14}, Z_{23}, Z_{24}, Z_{31}, Z_{32}, Z_{41}, and Z_{42} are equal to zero; $Z_{11} = Z_{22}$, $Z_{33} = Z_{44}$, $Z_{21} = Z_{12}$, and $Z_{34} = -Z_{43}$ (Mishchenko *et al.* 2000).

A.2. Results for BC spheres of different size in ice

To point out: (1) shifting of scattered intensity toward forward direction (small scattering angles) with increasing size. (2) Increasing number of angular oscillations with increasing size. (3) smallest particles have intensity distribution characteristics of dipole radiation (also known as Rayleigh scattering), (4) compared with Figure 16 and X=10 and X=100, the results for X=38.4 indicate that absorption effectively dampens the angular oscillations and reduces their frequency (see also Bohren *et al.* 1983). As shown in Figure 17 the peak between 120 and 150° is absent and oscillations are nearly smoothed out for scattering angles larger than 90°.

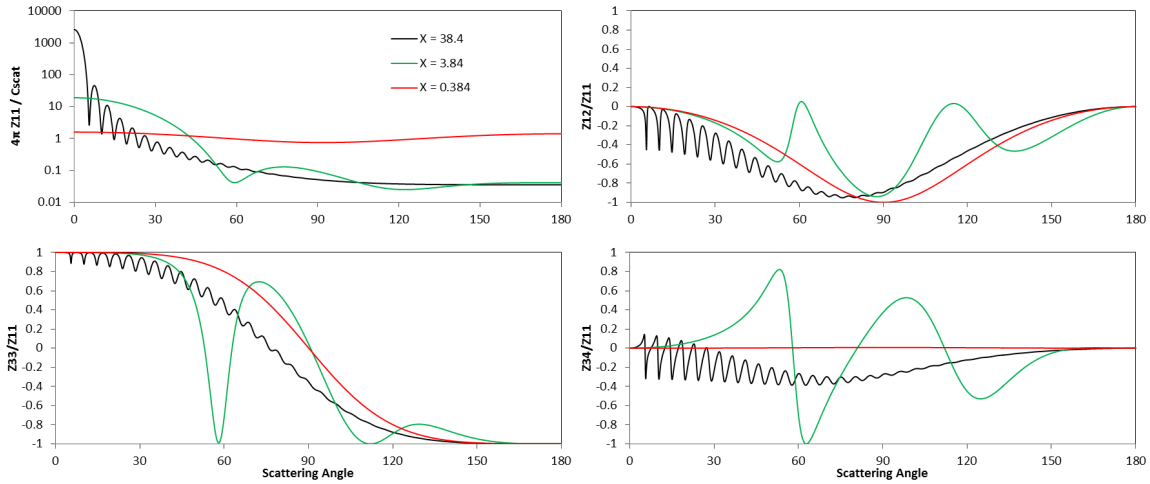

Figure 17. Angular distribution of scattered light by absorbing black carbon spheres embedded in ice. refractive indices m_{ice} = 1.3117 + i0.0, and m_{BC} = 1.54 + i0.37. Listed size parameters are effective parameters using the wavelength inside ice. The smallest size parameter X = 0.384 corresponds to a 30 nm sphere inside ice that is illuminated with 660 nm light.

APPENDIX B: THE ADDA CALCULATION

The number of dipoles per wavelength (dpl) describes the discretization resolution which controls the numerical accuracy of the calculation (Piller 1999; Ayrancı *et al.* 2007; Yurkin *et al.* 2007). To properly set dpl parameter in ADDA calculations, the basic requirement is that dipole size *d* should be smaller than both any structural length in the scatterer and the wavelength λ with the rule of thumb of 10 dipoles per wavelength inside the scatterer (Yurkin & Hoekstra 2013). While the wavelength criterion (in our case λ = 0.532 μm) can be easily fulfilled, the diameter of the included BC monomers, which is about 10 times smaller than the wavelength according to observations, also needs to be well characterized by the set-up dipole size. Therefore, a test on the dipole number per inclusion (dpi) is performed to see under what condition the output Mueller matrix from different dpi settings converges. All the elements of the output Mueller matrix have been examined, however only phase functions (P11) are shown as example (Figure 18). As illustrated below, the output P11, as well as other elements in the Mueller matrix, converges when dpi reaches 8. Therefore, in the all the following examinations, we adopted a second criterion in setting up dipole size -- dpi should be equal or larger than 8.

B.1. Orientation averaging

A comparison between four different DDA codes, including ADDA, DDSCAT, SIRRI and ZDD showed that ADDA is faster and the least memory consuming code and is superior in dealing with particles in single orientation (Penttilä *et al.* 2007). However, the orientation averaging of particles in ADDA is not that flexible, especially for a small number of sampling angles (Yurkin & Hoekstra 2013). Among the three Euler angles (α, β, γ) that specifies the particle orientation with respect to the laboratory reference frame (Yurkin & Hoekstra 2013), rotating over α is equivalent to rotating the scattering plane without changing the orientation of the scatterer relative to the incident radiation. ADDA employs the Romberg integrations (Davis & Rabinowitz 2007) for orientation averaging over β and γ. The Romberg integrations is potentially more accurate than, e.g., the Simpson rules employed by DDSCAT, but it requires more careful considerations of the particle shape in order to be used efficiently and is less flexible in the choice of number of orientations (Della Sala & D'Agostino 2013). In order to ensure the accuracy of the output, one should properly account for the particle symmetry, which is to adjust sampling range according to particle symmetry (the range of β and γ); as well as properly set ADDA orientation averaging scheme, which is to adjust sampling step (J_{max}) accordingly within the sampling range.

A quick test is carried out to explore an efficient way to set up orientation averaging parameters regarding the hexagonal prism shaped ice particles of interest (Table 4). Due to the natural geometry of hexagonal prism, x-y plane is a symmetry plane, therefore the range of β can be set to [0, 90] instead of [0, 180]; and every 60 degree of γ is a replication of itself assuming the particle is pure, therefore, the range of γ can be set to [0, 60] instead of [0, 360]. By reducing the angular range at both directions in orientation averaging, the execution time is brought down to at least one half of the original execution time. And for the simple case shown in the table, J_{max}, which determines the maximum times of averaging 2^{Jmax}, should be set to equal or larger than 4 for β and equal or larger than 3 for γ in order to reach convergence over both direction.

It should be noted that for ice crystal that contains BC inclusions at random locations, the symmetry plane doesn't apply anymore, so does the replication of every 60 degree over γ direction. As a result, full range averaging for these particles is required for both β and γ direction, and the J_{max} needs to be set to a larger value, e.g. 7, in order to guarantee convergence.

Table 4 Orientation averaging parameter settings and execution efficiency for hexagonal prism shaped pure ice crystal (diameter = 0.5 μm, length = 1 μm and aspect ratio = 2)

B	β - J_{max}	γ	γ - J_{max}	Convergence	Time (seconds)	Evaluations
[0, 180]	4	[0, 360]	4	β no	541	178
[0, 90]	3	[0, 360]	4	β no	291	97
[0, 90]	5	[0, 360]	4	yes	585	193
[0, 90]	5	[0, 60]	4	yes	247	81
[0, 90]	5	[0, 60]	3	yes	243	81
[0, 90]	5	[0, 60]	2	γ no	392	129
[0, 90]	4	[0, 60]	3	yes	240	81

B.2. Verification

Many studies have compared ADDA with other codes (see review by Yurkin & Hoekstra, 2007 and references there in). However, most of the studies focused on pure spherical particles which are not discussed in this paper. Bi *et al*. (2012) compared invariant imbedding method (IIM) and ADDA with large nonspherical inhomogeneous particles and found excellent agreement between the two methods. In this section, we processed the same particles presented in Bi *et al*. (2012) using ADDA under computational environment of this paper to see if same comparison results can be reached.

Figure 19 shows agreement between the two sets of results with minor differences which proves that the way utilizing ADDA code in this paper is in line with published results. The minor differences may be caused by the setting of dipole size as analyzed in Section 3.1, given there is no exact dipole size information in Bi *et al.* (2012).

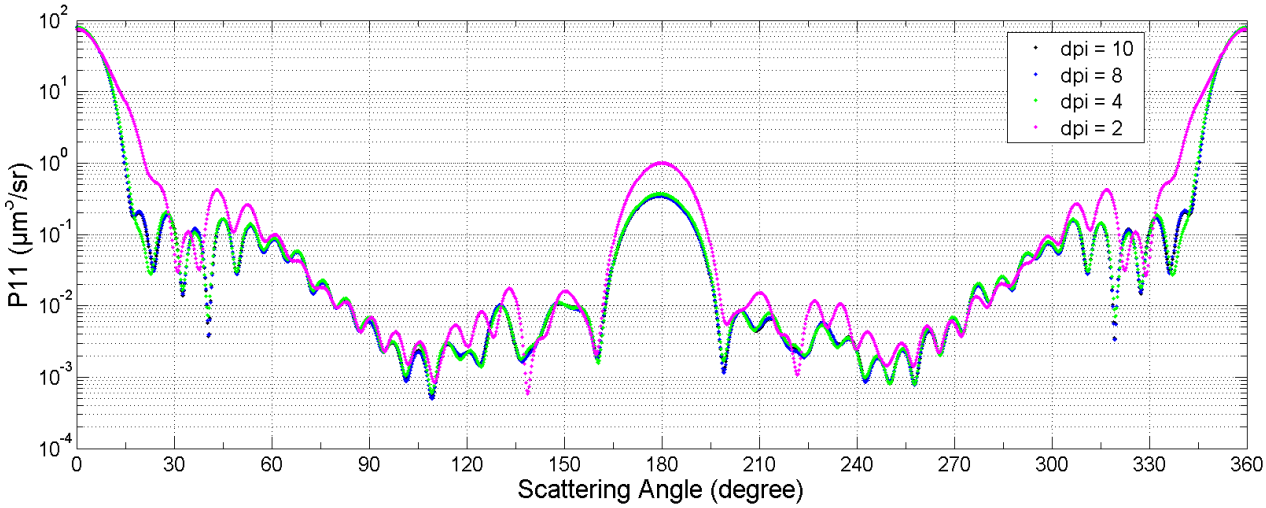

Figure 18 Comparison between phase functions (P11) using different dipole per inclusion (dpi) settings in ADDA. Input particles are hexagonal prism ice crystals (diameter = 2 μm, length = 4 μm, aspect ratio = 2) with 10 % total volume, same size (0.05 μm diameter), spherical BC monomers randomly distributed inside. The incident light at 0.532 μm is set to propagates from a fixed direction (0, 0, 1).

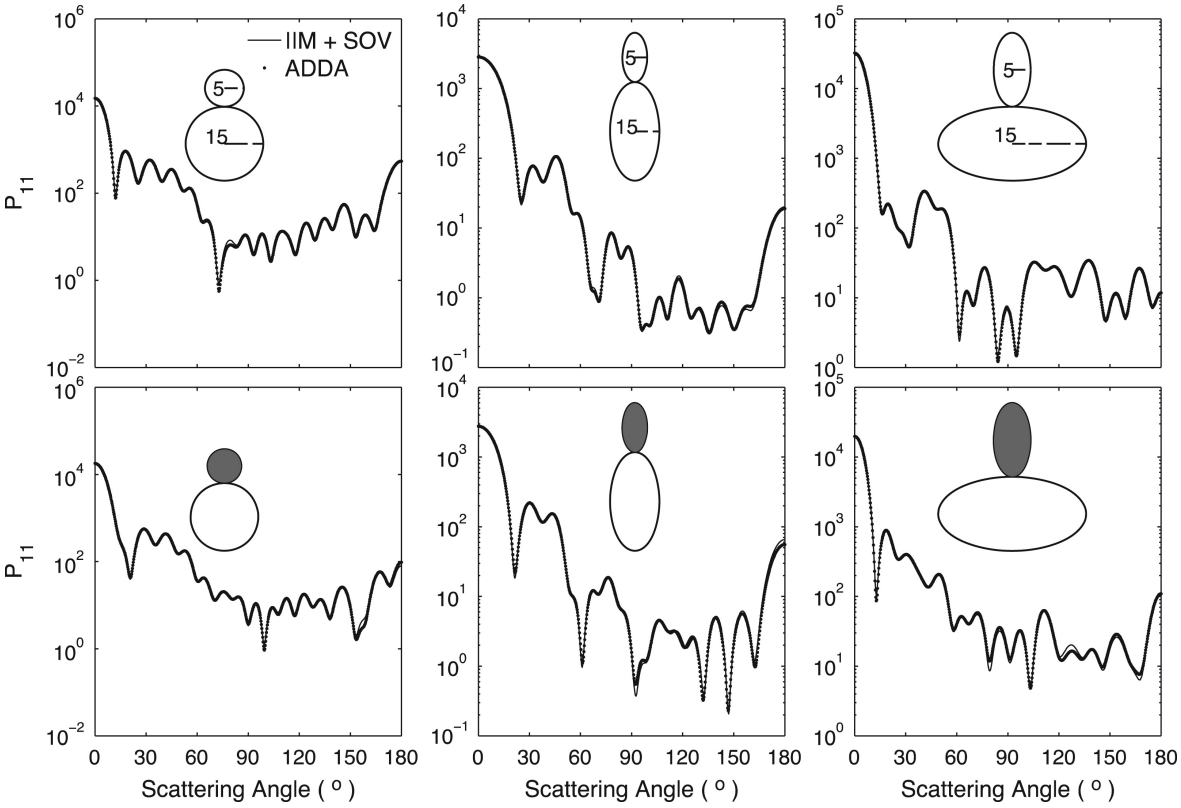

a)

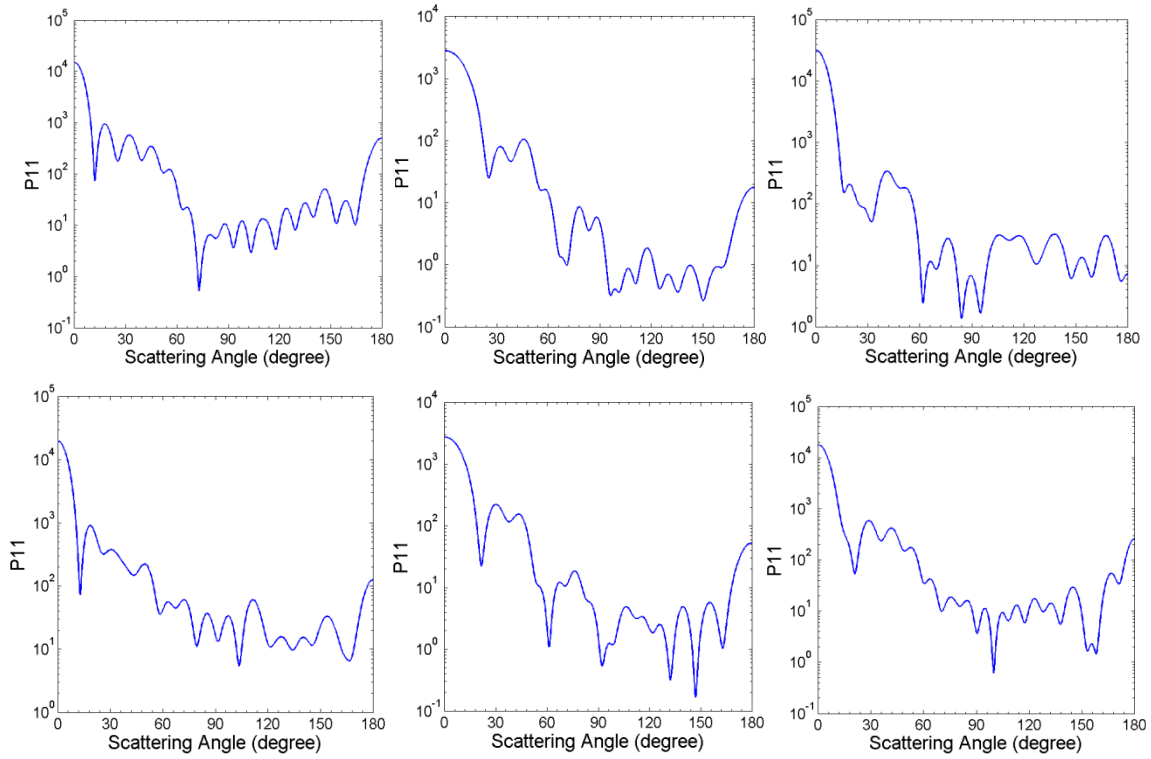
P11
Scattering Angle (degree)

b)

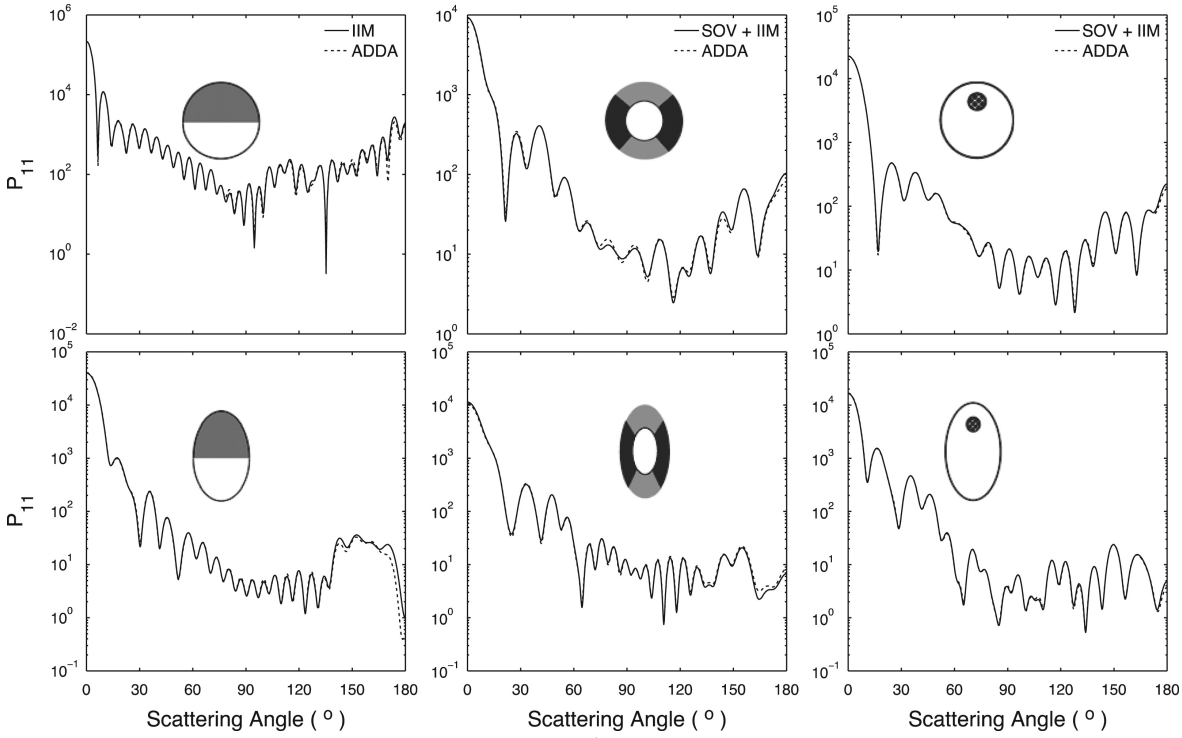
IIM
ADDA
SOV + IIM
ADDA
P11
Scattering Angle (º)

c)

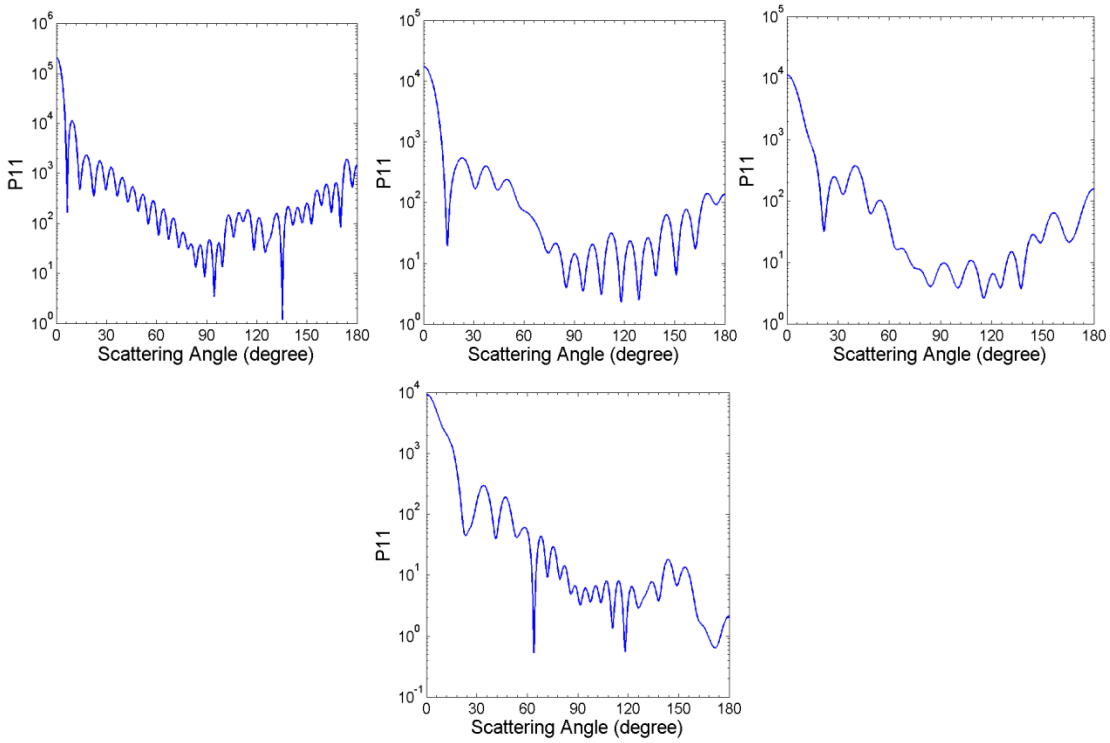

d)

Figure 19 Validation of phase functions (P11) using ADDA under computer environment of this paper with results in Bi *et al*. (2012). a) & c) Fig. 9 and Fig. 10 in Bi *et al*. (2012); b) & d) phase functions produced with input particles same with those showed in a) & c) at corresponding locations.

APPENDIX C: RADIATIVE EFFECTS OF SOOT IN CAM

The Community Atmosphere Model version 5 (CAM5) employs a modal aerosol module (MAM) to represent aerosols in multiple log-normally distributed modes, with a three-mode standard representation (MAM3) and a more complex seven-mode representation (MAM7). MAM7 resolves seven lognormal aerosol modes, keeping track of particle number concentration in each mode and internally-mixed mass concentrations of BC, sulfate, sea salt, primary and secondary organic matter, soil dust, and ammonium. The major difference between MAM3 and MAM7 related to carbonaceous aerosols lies in the treatment of BC aging. In MAM3, BC and primary organic matter (POM) particles are emitted into the accumulation mode (mid-size range of atmospheric aerosol), which also contains highly hygroscopic species such as sulfate and sea salt; in MAM7, BC and POM are emitted into a primary carbon mode, which contains no other species. BC is hydrophobic upon emission, and thus the hygroscopicity of the primary-carbon-mode particles depends on the assumed hygroscopicity for POM. As more hygroscopic species (e.g., H2SO4 and NH3) condense onto the primary-carbon-mode particles, the particles become more hygroscopic and are gradually transferred into the MAM7 accumulation mode.
In the accumulation mode of both MAM3 and MAM7, BC is internally mixed with other more hygroscopic species and is thus subject to wet scavenging and removal processes. Key processes associated with aerosol wet removal and convective transport can significantly influence the vertical distribution of aerosols and their transport to remote regions such as the Arctic.

Global emissions are used from all sectors for one BC mass mixing ratio variable. All physical and dynamic tendencies (e.g., transport, dry and wet removal) are calculated explicitly for as a single BC mass mixing ratio.

BC emissions from the different source regions and sectors might include monthly elevated open-fire emissions, and yearly constant surface emissions from shipping and from six sectors over land: agricultural waste burning, domestic, energy, industry, transportation, and waste treatment.

Attributing BC loading and radiative forcing to various regional/sectoral BC sources is important. It was found that BC lifetime, forcing-per-emission and forcing-per-loading have strong dependence on source regions.

DISTRIBUTION

[List external recipient names and addresses]

4 Lawrence Livermore National Laboratory
Attn: N. Dunipace (1)
P.O. Box 808, MS L-795
Livermore, CA 94551-0808

[List in order of lower to higher Mail Stop numbers.]

1	MSXXXX	Name of Person	Org. Number
1	MSXXXX	Name of Person	Org. Number

[The housekeeping entries are required for all SAND reports.]

1	MS0899	Technical Library	9536 (electronic copy)

For LDRD reports, add:

1	MS0359	D. Chavez, LDRD Office	1911

For CRADA reports add:

1	MS0115	OFA/NFE Agreements	10012

For Patent Caution reports, add:

1	MS0161	Legal Technology Transfer Center	11500


Sandia National Laboratories